

Unraveling the Complex Delithiation Mechanisms of Olivine-Type Cathode Materials, $\text{LiFe}_x\text{Co}_{1-x}\text{PO}_4$

Fiona C. Strobridge,[†] Hao Liu,^{†,||} Michal Leskes,^{†,⊥} Olaf J. Borkiewicz,[‡] Kamila M. Wiaderek,[‡] Peter J. Chupas,[‡] Karena W. Chapman,[‡] and Clare P. Grey^{*,†,§}

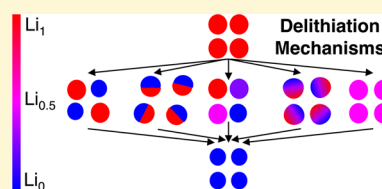
[†]Department of Chemistry, University of Cambridge, Lensfield Road, Cambridge, Cambridgeshire CB2 1EW, U.K.

[‡]X-ray Science Division, Advanced Photon Source, Argonne National Laboratory, Argonne, Illinois 60439, United States

[§]Department of Chemistry, State University of New York at Stony Brook, Stony Brook, New York 11794-3400, United States

Supporting Information

ABSTRACT: The delithiation mechanisms occurring within the olivine-type class of cathode materials for Li-ion batteries have received considerable attention because of the good capacity retention at high rates for LiFePO_4 . A comprehensive mechanistic study of the (de)lithiation reactions that occur when the substituted olivine-type cathode materials $\text{LiFe}_x\text{Co}_{1-x}\text{PO}_4$ ($x = 0, 0.05, 0.125, 0.25, 0.5, 0.75, 0.875, 0.95, 1$) are electrochemically cycled is reported here using in situ X-ray diffraction (XRD) data and supporting ex situ ^{31}P NMR spectra. On the first charge, two intermediate phases are observed and identified: $\text{Li}_{1-x}(\text{Fe}^{3+})_x(\text{Co}^{2+})_{1-x}\text{PO}_4$ for $0 < x < 1$ (i.e., after oxidation of Fe^{2+} to Fe^{3+}) and $\text{Li}_{2/3}\text{Fe}_x\text{Co}_{1-x}\text{PO}_4$ for $0 \leq x \leq 0.5$ (i.e., the Co-majority materials). For the Fe-rich materials, we study how nonequilibrium, single-phase mechanisms that occur discretely in single particles, as observed for LiFePO_4 at high rates, are affected by Co substitution. In the Co-majority materials, a two-phase mechanism with a coherent interface is observed, as was seen in LiCoPO_4 , and we discuss how it is manifested in the XRD patterns. We then compare the nonequilibrium, single-phase mechanism with the bulk single-phase and coherent interface two-phase mechanisms. Despite the apparent differences between these mechanisms, we discuss how they are related and interconverted as a function of Fe/Co substitution and the potential implications for the electrochemistry of this system.



1. INTRODUCTION

Since the initial publication by Padhi et al. in 1997 on LiFePO_4 ,¹ the olivine family has been extensively researched as potential cathode materials for Li-ion batteries. LiFePO_4 's high stability, long cycle life, good reversibility,² and safe operating voltage (3.45 V vs Li^+/Li) have led to its use in commercial batteries. While LiFePO_4 has been widely studied, the mechanism by which it is transformed during electrochemical cycling is not trivial. The transformation mechanisms for the substituted and in principle higher-energy density variants $\text{LiFe}_x\text{M}_{1-x}\text{PO}_4$ ($\text{M} = \text{Mn}, \text{Co}, \text{Ni}; 0 \leq x \leq 1$) are even more complex and generally not well understood. Understanding how Li is deintercalated and reintercalated upon charging and discharging, respectively, is fundamental to explaining the electrochemical properties of known electrode materials and essential to help develop new electrode materials. Specifically, substitution of Mn, Co, and Ni generally results in poorer performance in terms of rate and capacity, but this is not true of all levels of metal substitution. It is therefore important to understand why some compositions show improved performance and others do not.

Here we use time-resolved in situ synchrotron X-ray diffraction methods to explore systematically how Co substitution in LiFePO_4 alters the structural transformations that occur upon cycling for the entire $\text{LiFe}_x\text{Co}_{1-x}\text{PO}_4$ phase diagram. We start by describing the possible relevant (de)lithiation mechanisms proposed for $\text{LiFe}_x\text{M}_{1-x}\text{PO}_4$ and how they are, or would be, manifested in the X-ray diffraction (XRD) data (Figure 1) in order to help in the

interpretation of the in situ XRD data for the $\text{LiFe}_x\text{Co}_{1-x}\text{PO}_4$ series presented in this paper.

Initially, XRD and transmission electron microscopy (TEM) studies carried out on micron-sized LiFePO_4 particles identified a two-phase reaction mechanism (A) (illustrated in Figure 1) in which both end-member phases (LiFePO_4 and FePO_4) are present, separated by a coherent interface within a single particle, at intermediate states of charge.^{1,3} This mechanism is observed as the simultaneous disappearance and growth of the XRD reflections of the reactant and product phases, respectively. Although micron-sized particles can be chemically delithiated, their electrochemical performance is poor. LiFePO_4 (space group $Pnma$) has one-dimensional Li diffusion channels in the b direction,⁴ and its electrochemical performance was found to significantly improve when the particles were nanosized.⁵ The decrease in particle size also leads to a change in the reaction mechanism since the high-energy interface between LiFePO_4 and FePO_4 is no longer stable within a single nanoparticle and only fully lithiated and fully delithiated particles could be detected in ex situ XRD studies upon cycling.⁶ These findings were explained by Delmas et al.⁶ in their domino-cascade model (B), in which the reaction occurs particle-by-particle (as shown in Figure 1), resulting in sequential, heterogeneous delithiation

Received: January 24, 2016

Revised: April 24, 2016

Published: April 25, 2016

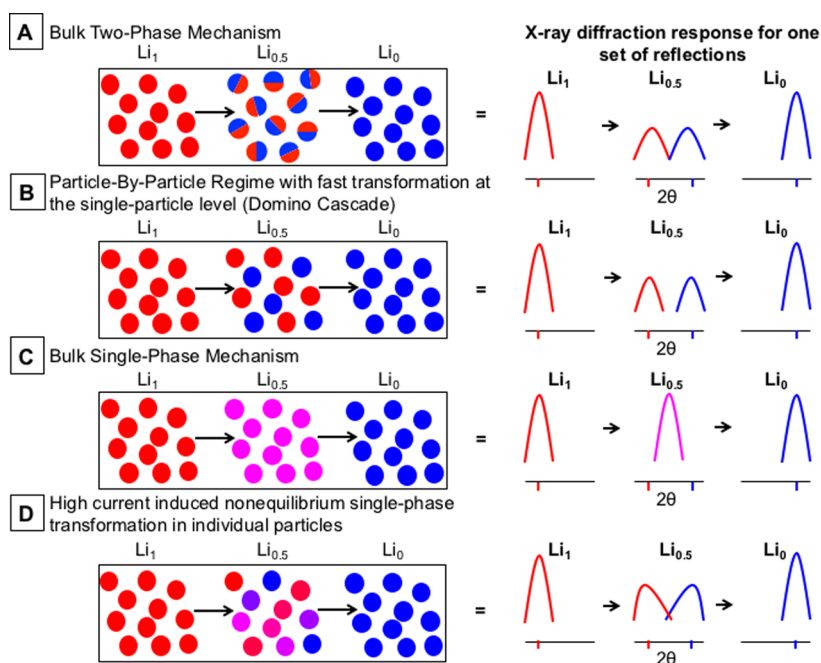


Figure 1. Simplified illustration of five different possible delithiation schemes for the olivine materials and their resulting in situ XRD responses for a single reflection (such as the 020 reflection) at the compositions Li_1 , $\text{Li}_{0.5}$, and Li_0 (i.e., LiMPO_4 , $\text{Li}_{0.5}\text{MPO}_4$ and MPO_4): (A) the bulk two-phase mechanism in which both phases coexist in a single particle; (B) the particle-by-particle reaction regime, where the particles exist only as either Li_1 or Li_0 ; (C) the bulk single-phase mechanism; (D) the nonequilibrium single-phase transformation occurring sequentially particle-by-particle; (E) the two-phase mechanism with a coherent interface, explored in more detail in this paper.

of the particles in the electrode. It was proposed that the particles still undergo a two-phase mechanism, but since the interface is energetically unfavorable, it propagates very quickly within each particle. It should be noted that as a result of the added strain at the phase boundary that exists during reaction scheme A, the full widths at half-maximum of specific classes of reflections in the diffraction experiment are expected to be larger than if the two phases exist in different particles, such as in scheme B (as illustrated in Figure 1). Recent soft X-ray ptychography combined with X-ray absorption spectroscopy and TEM measurements have shown that LiFePO_4 and FePO_4 can coexist in particles as small as 100 nm.⁷

The good capacity retention at exceptionally high rates for LiFePO_4 nanoparticles⁸ is in apparent contradiction with a two-phase mechanism: two-phase mechanisms typically result in high activation energy barriers for the nucleation and growth of a new phase. Although the Li solubility in $\text{Li}_{1-\delta}\text{FePO}_4$ and $\text{Li}_{1-\delta}\text{FePO}_4$ increases as the particle size decreases, there is still a miscibility gap even for 34 nm particles.⁹ Density functional theory calculations by Malik et al.¹⁰ predicted that a single-phase transformation is accessible when an overpotential is applied to nanosized LiFePO_4 . Ferguson and Bazant¹¹ proposed, on the basis of their simulations, that metastable solid-solution phases arise from kinetic suppression of the phase separation. These proposals are supported by our in situ XRD studies¹² and those of Zhang et al.,¹³ which captured metastable structures extending across the whole Li_yFePO_4 composition range ($0 \leq y \leq 1$) at high cycling rates. The metastable structures were observed as an asymmetric broadening of the Bragg reflections of the end-member phases toward each other (scheme D in Figure 1), resulting in the reflections forming one continuous peak. Our simulations of the diffraction data showed that this asymmetric broadening could not be modeled within a simple coherent interface model (scheme E).^{12,14} In practice it is difficult to determine whether some of the broadening originates from the existence of multiple interphases

within one particle.^{12,15} However, at lower charge rates, since the nanosized LiFePO_4 particles react very quickly (a few particles at a time), the patterns from the two end-member phases dominate the XRD response, and the response is essentially indistinguishable from that seen for scheme B in Figure 1.¹⁶ The nonequilibrium single-phase mechanism (D) should be contrasted to that expected for a thermodynamically stable solid solution, where the peaks shift continuously from those of the fully lithiated to the fully delithiated phase (scheme C in Figure 1). If in scheme A (the bulk two-phase reaction) there is some coherency at the interface, there will be a distortion at the interface of the two phases to reduce the strain, leading to the final scheme, the coherent interface model (E). The subtle differences between schemes E and A and how they are manifested in the in situ powder XRD patterns of the nanoparticulate olivine materials will be discussed in detail in this paper.

Here, to explore the delithiation mechanisms occurring within the olivine class of cathode materials, we study the $\text{LiFe}_x\text{Co}_{1-x}\text{PO}_4$ series ($x = 0, 0.05, 0.125, 0.25, 0.5, 0.75, 0.875, 0.95, 1$). Complex in situ XRD patterns are generally observed for nanoparticulate cation-substituted olivine materials upon cycling, with both solid-solution and two-phase behavior at low cycle rates,^{14,17} suggesting that the mechanism of (de)lithiation deviates from those of the nonsubstituted materials. For example, in the Mn-substituted series $\text{LiFe}_x\text{Mn}_{1-x}\text{PO}_4$, an intermediate phase, $\text{Li}_y\text{Fe}_x\text{Mn}_{1-x}\text{PO}_4$, was observed in the in situ XRD patterns and exhibited a larger Li solubility than the end members, $\text{LiFe}_x\text{Mn}_{1-x}\text{PO}_4$ and $\text{Fe}_x\text{Mn}_{1-x}\text{PO}_4$.¹⁴ A two-phase mechanism between $\text{LiFe}_x\text{Mn}_{1-x}\text{PO}_4$ and $\text{Li}_y\text{Fe}_x\text{Mn}_{1-x}\text{PO}_4$ was observed upon charge, but a bulk single-phase transformation (mechanism C) between the two phases was then seen upon discharge. Substitution on the transition metal site in the olivine cathode materials is thought to facilitate the single-phase mechanism,^{17–19} helping to improve the rate performance of

the cathode materials, as demonstrated in vanadium-substituted LiFePO_4 .²⁰

Very different mechanisms are observed for the Co-containing olivines: Ehrenberg and co-workers observed by in situ XRD that the delithiation mechanism of the end member LiCoPO_4 occurs via a Li_yCoPO_4 intermediate with two distinct reactions occurring: $\text{LiCoPO}_4 \rightarrow \text{Li}_y\text{CoPO}_4$ and $\text{Li}_y\text{CoPO}_4 \rightarrow \text{CoPO}_4$.^{21,22} The processes result in significant loss of long-range order.²³ In our previous study using in situ XRD and ex situ NMR spectroscopy,²⁴ we showed that the intermediate phase has the composition $\text{Li}_{2/3}(\text{Co}^{3+})_{1/3}(\text{Co}^{2+})_{2/3}\text{PO}_4$, its structure being obtained by an $(a \times 3b \times c)$ supercell expansion of the primitive olivine unit cell. Here we systematically monitor the changes in the in situ XRD patterns for high and low substitution levels of both Fe and Co and then analyze how these changes can be understood within the different delithiation reaction schemes (using Figure 1 as a guide). This allows us to develop a systematic understanding of how substitution affects the complex reaction mechanisms in this series.

We first present XRD characterization of the as-synthesized materials in the $\text{LiFe}_x\text{Co}_{1-x}\text{PO}_4$ series (section 3.1). We then consider Fe-rich $\text{LiFe}_x\text{Co}_{1-x}\text{PO}_4$ ($x \geq 0.875$) and use whole-powder-pattern fitting as described by Liu et al.¹² to study the first 1.5 cycles (section 3.2). We next study the highly substituted materials, $\text{LiFe}_{0.5}\text{Co}_{0.5}\text{PO}_4$ and $\text{LiFe}_{0.25}\text{Co}_{0.75}\text{PO}_4$, and identify the intermediates that are formed upon charging the cosubstituted olivines (section 3.3). Relevant NMR spectra are presented to confirm the bulk oxidation changes. Using XRD patterns, refinements, and simulations, we discuss in detail the nature of any coherent interfaces formed during a two-phase reaction and explain how they are manifested in the XRD patterns. We compare the delithiation mechanisms for the transformations between the starting, intermediate, and final phases as a function of Co content. We show that the relationships between the different mechanisms are determined by the length of the coherent interface, the ability of the material to tolerate intermediate Li compositions, the extent of disorder of Li^+ /vacancies and $\text{Fe}^{3+}/\text{Co}^{2+}$, and the change in volume between the two end-member phases. From the study of the whole series, trends emerge that were not apparent when single compositions were investigated individually.

2. EXPERIMENTAL DETAILS

2.1. Solid-State Synthesis of $\text{LiFe}_x\text{Co}_{1-x}\text{PO}_4$. The carbon-coated series $\text{LiFe}_x\text{Co}_{1-x}\text{PO}_4$ ($x = 1, 0.95, 0.875, 0.75, 0.5, 0.25, 0.125, 0.05, 0$) were synthesized via the solid-state method using iron oxalate (Sigma-Aldrich, 99.997%), cobalt oxalate (Sigma-Aldrich), lithium carbonate (Sigma-Aldrich, 99.997%), ammonium dihydrogen phosphate (Sigma-Aldrich, 99.999%), and 10 wt % Ketjen black (AzkoNobel) in stoichiometric mixtures. After high-energy ball milling for 20 min, each reaction mixture was pelletized and heated to 600 °C under flowing argon. For $x = 1, 0.95$, and 0.875 , the precursors were heated for 6 h.²⁵ For $x = 0.75$, they were heated for 6 h, cooled, and reheated for a further 11 h. For $\text{LiFe}_x\text{Co}_{1-x}\text{PO}_4$ ($x = 0.5, 0.25, 0.125, 0.05, 0$), the precursors were heated for 6 h and then cooled and reheated twice for 11 h before a final 24 h heating step. The additional heating and cooling steps were carried out to decrease the amount of impurities present in the final product.

2.2. Film Fabrication and Battery Assembly for the in Situ XRD Studies. The electrode was prepared by grinding 85 wt % carbon-coated $\text{LiFe}_x\text{Co}_{1-x}\text{PO}_4$, 5 wt % Super P carbon (Alfa Aesar), 5 wt % carbon black (Vulcan XC-72, Cabot Corporation), and 5 wt % polytetrafluoroethylene (PTFE) (Sigma-Aldrich) in a mortar and pestle. The powder was pressed into a 13 mm diameter pellet with a thickness of $\sim 150 \mu\text{m}$ and a mass of $\sim 22 \text{ mg}$. The AMPIX²⁶ cell was assembled in an argon-filled glovebox using Li metal as the counter electrode, a Whatman GF/B borosilicate microfiber filter as the separator, and a 1 M solution of LiPF_6

in a 1:1 mixture of ethylene carbonate/dimethyl carbonate as the electrolyte (Tomiyama Pure Chemical Industries).

2.3. In Situ XRD. In situ XRD experiments were performed at the powder diffraction beamline, 11-BM, at the Advanced Photon Source (APS) at Argonne National Laboratory (ANL) using a 12-channel analyzer detector array ($\lambda = 0.413609 \text{ \AA}$, beam size $1.5 \text{ mm} \times 0.5 \text{ mm}$).²⁷ Data spanning a 2θ range of $0\text{--}26^\circ$ were collected using a step size of 0.002° . To increase the experiment throughput, multiple batteries were assembled on a motorized stage and translated into the X-ray beam periodically for diffraction measurements. For $x = 0.95, 0.875, 0.125$, and 0.05 , each measurement took 10 min 42 s (using a time per step of 0.34 s), and scans were obtained every 60 min 25 s. For $x = 1, 0.75, 0.5, 0.25$, and 0 , more scans were acquired during parts of the electrochemical cycling where large structural changes had been observed to occur in earlier preliminary measurements on these samples. All of these scans took 7 min 40 s (the time per step was 0.23 s). Since the sampling of the electrochemical processes was nonuniform for these batteries, the points where scans were taken are shown in Figures S1 and S2 in the Supporting Information (SI) and in the main text (for the first charge) as indicated in the figure captions. All of the batteries for the in situ XRD experiments were galvanostatically cycled at a rate of $C/20$ using a Maccor model 4300 cycler. The current was continuously applied while the samples were automatically moved in and out of the beam on the sample stage, so that they did not have a chance to “relax”. A rate of $C/20$ was used for three reasons: (a) The scan time for one XRD pattern took 10 min 42 s (for $x = 1, 0.75, 0.5, 0.25$, and 0), which at a rate of $C/20$ corresponds to change in state of charge of $<0.9\%$, which we thought was small enough to result in minimal peak broadening or other artifacts. (b) Since we were studying six cells simultaneously, with scans taking 10 min 42 s, if we cycled at $C/20$, we could collect on average ~ 20 data points on the charge. As these materials are known for having more than one plateau, we felt that it was important to collect as many data points as realistically possible. (c) We wanted all of the materials to reach highly charged states (i.e., to remove as much Li as possible), and since the Co-containing materials show poorer electrochemistry than LiFePO_4 at higher rates, we chose a moderately low cycle rate. Rietveld refinements were performed using the Topas Academic software.²⁸ The individual XRD patterns, Rietveld refinements, and difference plots for patterns from the in situ XRD data for LiFePO_4 during the first charge at 8%, 57%, and 99% state of charge are shown in Figure S3.

2.4. Whole-Powder-Pattern Fitting of the in Situ XRD Patterns. The same method as discussed in our earlier paper¹² was used in this study. The background was described by the Chebyshev polynomial. The instrumental broadening was assumed to be negligible and was not considered in the refinement; hence, the broadening of the diffraction peak was attributed solely to the size and strain effects of the sample.

A Lorentzian peak profile was used to model the size broadening, and the apparent size was assumed to be isotropic with respect to different hkl reflections. The dependence of the full width at half-maximum (fwhm), β , on θ is given by

$$\beta = \frac{\lambda}{L \cos \theta_{hkl}} \quad (1)$$

where λ is the wavelength and L is the refined apparent size parameter. The strain/compositional effect was described by a convolution of symmetrical and asymmetrical profile functions. A Gaussian profile peak function was chosen to model the symmetrical broadening due to strain, and this strain was also assumed to be isotropic with respect to different hkl reflections. The θ dependence of the fwhm is given by

$$\beta = E \tan \theta_{hkl} \quad (2)$$

where E is the refined symmetrical strain parameter. The asymmetrical profile was modeled using an exponential function:

$$f(\theta) = \exp\left(-\frac{2\theta - 2\theta_{hkl}}{\varepsilon_m}\right) \quad (3)$$

where ε_m is the refined parameter and θ is defined in the range $[\theta_{hkl}, +\infty]$ for $\varepsilon_m > 0$ and $[-\infty, \theta_{hkl}]$ for $\varepsilon_m < 0$. Because of the anisotropic changes

in the lattice parameters going from $\text{LiFe}_x\text{Co}_{1-x}\text{PO}_4$ to $\text{Fe}_x\text{Co}_{1-x}\text{PO}_4$, where a and b contract and c expands, we had to include an hkl -dependent description of the asymmetrical profile, which was done by including a symmetrized spherical harmonics series in ε_m :

$$\varepsilon_m = \sum_{ij} C_{ij} Y_{ij}(\omega, \varphi) \tan \theta_{hkl} \quad (4)$$

where $Y_{ij}(\omega, \varphi)$ are the symmetrized spherical harmonics^{29,30} and C_{ij} are the refined parameters.

The pure strain-induced profile for a certain hkl reflection was obtained by convoluting the symmetrical Gaussian function and the exponential function defined at the corresponding θ_{hkl} . This convoluted profile corresponds to the variation of the lattice parameters. The population density function (pdf) on the 2θ scale for an hkl interplanar spacing of one phase is given by

$$\text{pdf}(2\theta)_{hkl} = \frac{1}{E\sqrt{2\pi}} e^{-(2\theta-2\theta_{hkl})^2/2E^2} \otimes f(\theta) \quad (5)$$

where E is the refined symmetrical strain parameter defined in eq 2 and $f(\theta)$ is given by eq 3. The population densities of the a , b , and c lattice parameters for one phase are given by pdf_{200} , pdf_{020} , and pdf_{002} , respectively. The total population density (considering both Li-rich and Li-poor phases) is given by

$$\text{pdf}(2\theta) = \text{SF}_1 \times \text{pdf}(2\theta)_{hkl,1} + \text{SF}_2 \times \text{pdf}(2\theta)_{hkl,2} \quad (6)$$

where SF_1 and SF_2 are the scale factors for the Li-rich and Li-poor phases, respectively. Bragg's law was used to convert the scale from 2θ to d -spacing.

The whole-powder-pattern fitting of the in situ diffraction patterns within the 2θ range between 3.5° and 15° was carried out sequentially using the TOPAS structural refinement package.³¹

2.5. Simulations of XRD Peak Profiles for a Coherent Interface. A cubic particle with edges parallel to the a , b , and c axes of the olivine crystal structure was used for the simulation. Each edge was 100 nm long. The interface was assumed to be perpendicular to the $[h00]$ direction, and the Li concentration and lattice parameter profiles along the $[h00]$ direction were assumed to take the following form:

$$a(x) = \frac{a_0 + a_1}{2} + \frac{a_1 - a_0}{2} \tanh\left(\frac{2}{L}(x - x_0)\right) \quad (7)$$

where a_0 and a_1 represent the values of the quantity (Li concentration or lattice parameter) for the two end-member phases, respectively, L is the width of the interface, x_0 is the central position of the interface, and x is the coordinate along the $[h00]$ direction. The delithiation process was simulated in discrete steps by varying x_0 from one end of the particle to the other. The value of x_0 was determined in such a way as to make sure the global Li concentration was consistent with the state of charge.

The X-ray diffraction intensity was simulated following the treatment by Warren.³² For a $0k0$ reflection, the diffraction power as a function of diffraction angle 2θ can be expressed as

$$P(2\theta) = \frac{K}{\sin^2 \theta} \sum_{m'} \sum_m f_m f_{m'} e^{(2\pi i/\lambda)(2 \sin \theta)(R_{m'} - R_m)} \quad (8)$$

where the subscripts m and m' represent the indices of the unit cells, f_m is the structure factor of unit cell m , R_m is the position coordinate of unit cell m , λ is the X-ray wavelength, and K is a factor independent of θ . The summation is performed over all of the unit cells in the particle. The structure factor f for the 020 reflection was assumed to vary linearly with the Li composition c :³³

$$f(c) = (1 - c)f(0) + cf(1) \quad (9)$$

where $f(0)$ is the structure factor for the 020 reflection of $\text{Fe}_{0.25}\text{Co}_{0.75}\text{PO}_4$ and $f(1)$ is that for $\text{LiFe}_{0.25}\text{Co}_{0.75}\text{PO}_4$.

3. RESULTS AND DISCUSSION

3.1. Synthesis and Characterization of $\text{LiFe}_x\text{Co}_{1-x}\text{PO}_4$.

The carbon-coated $\text{LiFe}_x\text{Co}_{1-x}\text{PO}_4$ ($x = 0, 0.05, 0.125, 0.25, 0.5,$

$0.75, 0.875, 0.95, 1$) materials were synthesized via solid-state synthesis. Additional heating steps were required for higher Co compositions to decrease the extent of impurities present in the product (including Li_3PO_4 , as shown in Figure S4).²⁵ The average particle size of LiFePO_4 is approximately 120 nm, as determined from scanning electron microscopy (SEM) images of a LiFePO_4 electrode taken at different magnifications (shown in the SI). The large distribution of particle sizes (from ~ 50 to 350 nm) and spherical-type morphology are expected for the solid-state synthesis.^{34,35} SEM images of the as-synthesized carbon-coated LiCoPO_4 powder indicate that the particle size is smaller than 50 nm (see Figure S5). Therefore, the particle sizes of all of the $\text{LiFe}_x\text{Co}_{1-x}\text{PO}_4$ compositions are assumed to be in the nanoparticle regime.

3.2. Fe-Rich $\text{LiFe}_x\text{Co}_{1-x}\text{PO}_4$ ($x = 1, 0.95, 0.875$). **3.2.1. First Charge.** In situ XRD patterns of the Fe-rich substituted olivines (LiFePO_4 , $\text{LiFe}_{0.95}\text{Co}_{0.05}\text{PO}_4$, and $\text{LiFe}_{0.875}\text{Co}_{0.125}\text{PO}_4$) cycled at a rate of C/20 for the first cycle and up to 100 $\text{mA h}^{-1} \text{g}^{-1}$ of the second charge are presented in Figure 2a–c, respectively. The 2θ range in Figure 2a–c shows the 020 and 211 reflections of the lithiated and delithiated phases. Only the FePO_4 and LiFePO_4 reflections are observed when LiFePO_4 is charged at this low rate (Figure 2a). This is characteristic of a “two-phase reaction” at the electrode level, the delithiated phase being formed at the expense of the fully lithiated phase with no significant peak shift and broadening (as discussed in the Introduction). We cannot determine the exact mechanism of the reaction at the single-particle level, i.e., we cannot distinguish whether two phases exist within the same particles or in different particles, at intermediate states of charge, as depicted in schemes A and B in Figure 1,^{6,10} because of the limited resolution of the experimental setup and the limited fraction of the sample that is expected to be undergoing a transformation (delithiation) at one time at the low rates used here.

In both $\text{LiFe}_{0.95}\text{Co}_{0.05}\text{PO}_4$ and $\text{LiFe}_{0.875}\text{Co}_{0.125}\text{PO}_4$, the evolution of the intensities and positions of the reflections of the end-member lithiated phase on charging is similar to that observed for LiFePO_4 . In contrast, the peak positions of the delithiated phases deviate noticeably from the positions of $\text{Fe}_x\text{Co}_{1-x}\text{PO}_4$, shifting toward that of the Li_0 phase as charging proceeds. The extent of the deviations becomes more significant as the Co content increases.

Rietveld refinements were carried out using the XRD data, and the changes in the unit cell volumes as a function of capacity are plotted in Figure 2d–f. The theoretical capacity of $\text{LiFe}_x\text{Co}_{1-x}\text{PO}_4$ is between 167 and 170 $\text{mA h}^{-1} \text{g}^{-1}$. However, as shown in Figure 2e,f, the charge capacities for the Co-containing materials are noticeably larger than expected as a result of side reactions (potentially including oxidation of the electrolyte above 4.6 V, the formation of a solid electrolyte interphase (SEI) at the cathode,^{36,37} metal dissolution,³⁸ and oxidation of carbon). Nevertheless, the discharge capacities are among the highest recorded for these materials ($\sim 160 \text{ mA h}^{-1} \text{g}^{-1}$; Table S1 and Figure S6), suggesting that the reversibility of the electrochemical reactions is not significantly affected by the side reactions, at least in the first few cycles.

Since the $\text{Fe}^{2+} \rightarrow \text{Fe}^{3+}$ and $\text{Co}^{2+} \rightarrow \text{Co}^{3+}$ redox reactions occur at ~ 3.5 and ~ 4.8 V, respectively, in the olivine structure, Fe^{2+} is oxidized first upon charging. Therefore, the particles must have a Li content of $\text{Li}_{1-x}\text{Fe}_x\text{Co}_{1-x}\text{PO}_4$ at the end of the 3.6 V process because $x\text{Li}$ per formula unit is deintercalated during the Fe plateau. A continual and gradual shift of the unit cell volume is observed going from the $\text{Li}_{1-x}(\text{Fe}^{3+})_x(\text{Co}^{2+})_{1-x}\text{PO}_4$ phase to the fully delithiated $(\text{Fe}^{3+})_x(\text{Co}^{3+})_{1-x}\text{PO}_4$ material upon charging at >3.5 V

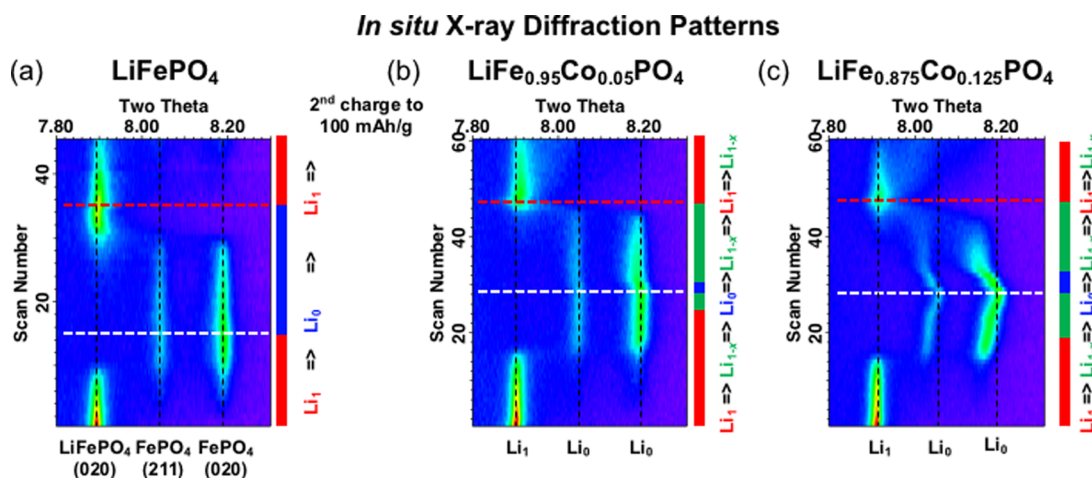


Figure 2. In situ XRD data for the first cycle and up to $100 \text{ mA h}^{-1} \text{ g}^{-1}$ of the second charge of the Fe-rich $\text{LiFe}_x\text{Co}_{1-x}\text{PO}_4$ phases ($x = 1, 0.95,$ and 0.875 in (a–c), respectively) while cycling at a rate corresponding to $C/20$. Here and in all of the XRD patterns presented in this paper, the x axis displays the 2θ region = $7.8\text{--}8.3^\circ$ ($\lambda = 0.413609 \text{ \AA}$), showing the characteristic 020 and 211 reflections of the end-member phases. The y axis represents the scan number. These scan numbers correspond to the red crosses (and blue boxes) marked on the electrochemical data in (d–f). The black dotted vertical lines indicate the positions of the peaks of the fully lithiated and delithiated phases. Unit cell volume changes as a function of capacity (in $\text{mA h}^{-1} \text{ g}^{-1}$) for $x = 1, 0.95,$ and 0.875 are shown in (d)–(f), respectively. The black line represents the electrochemistry, while the red crosses, blue squares represent the volumes of the $\text{LiFe}_x\text{Co}_{1-x}\text{PO}_4$, $\text{Fe}_x\text{Co}_{1-x}\text{PO}_4$ phases, respectively. Variations of the b lattice parameter, plotted as the population density, as a function of the scan number for $x = 1, 0.95,$ and 0.875 are shown in (g–i) respectively (extracted from refinements using whole-powder-pattern fits). The b lattice parameters for the lithiated and delithiated phases are ~ 6.0 and 5.8 \AA , respectively. The (a–c) white and (g–i) black dashed horizontal lines indicate the end of the charge, while the red dashed lines represent the end of the discharge. The red, green, and blue bars alongside the figure show when the Li_{1-x} , Li_{1-x} , and $\text{Li}_0\text{Fe}_x\text{Co}_{1-x}\text{PO}_4$ phases, respectively, are being consumed.

(Figures 2e,f), which is indicative of a single-phase transition between the two Li stoichiometries at the bulk (electrode) level (mechanism C) for the $\text{Co}^{2+}/\text{Co}^{3+}$ process. Ex situ ^{31}P NMR spectra of the fully charged material confirm the complete transformation of these phases to $\text{Fe}_x\text{Co}_{1-x}\text{PO}_4$ (Figure S7).

3.2.2. Subsequent Cycles: The Discrete Nonequilibrium Single-Phase Mechanism (D). As shown in Figure 2a–c the first discharge and second charge appear to have different in situ XRD responses compared with the first charge. The sharp reflections from the pristine structure are not reformed after the first cycle, instead, the reflections are broader and asymmetric (the individual diffraction patterns are plotted in Figure S8). Additionally, low-intensity, continually shifting peaks are observed between the $\text{LiFe}_x\text{Co}_{1-x}\text{PO}_4$, $\text{Li}_{1-x}\text{Fe}_x\text{Co}_{1-x}\text{PO}_4$, and $\text{Fe}_x\text{Co}_{1-x}\text{PO}_4$ reflections in the first discharge and second charge, which correspond to compositions with intermediate stoichiometries. The patterns qualitatively resemble those observed by Liu et al.¹² during very fast cycling of LiFePO_4 , this phenomenon being attributed to the nonequilibrium single-phase, particle-by-particle delithiation mechanism of LiFePO_4 (mechanism D).

Following the work of Liu et al.,¹² we used whole-powder-pattern fitting to obtain population densities describing the fractions of the sample exhibiting different cell parameters. The population densities of the b lattice parameters for LiFePO_4 , $\text{LiFe}_{0.95}\text{Co}_{0.05}\text{PO}_4$, and $\text{LiFe}_{0.875}\text{Co}_{0.125}\text{PO}_4$ plotted as a function of scan number for the first 1.5 cycles are shown in Figure 2g–i, respectively. Liu et al.¹² observed that $\text{Li}_{1-\delta}\text{FePO}_4$ can accommodate a larger deviation in the a , b , and c lattice parameters from the end member LiFePO_4 than $\text{Li}_\delta\text{FePO}_4$ can from FePO_4 (after the first charge). This is supported by phase-field simulations³⁹ and in situ XRD experiments,^{25,40} both of which show that $\text{Li}_{1-\delta}\text{FePO}_4$ is able to exist in a larger single-phase region than $\text{Li}_\delta\text{FePO}_4$. When 5% Co is substituted onto the Fe site, the $\text{Li}_{0.95}\text{Fe}_{0.95}\text{Co}_{0.05}\text{PO}_4$ intermediate can tolerate an even larger range of cell parameters beyond those observed for $\text{LiFe}_{0.95}\text{Co}_{0.05}\text{PO}_4$ and

$\text{Fe}_{0.95}\text{Co}_{0.05}\text{PO}_4$. This becomes apparent upon discharge. The effect is more pronounced for $\text{LiFe}_{0.875}\text{Co}_{0.125}\text{PO}_4$, which upon discharge first shows bulk single-phase (solid solution) behavior (mechanism C) between fully delithiated $\text{Fe}_{0.875}\text{Co}_{0.125}\text{PO}_4$ and the intermediate $\text{Li}_{0.125}\text{Fe}_{0.875}\text{Co}_{0.125}\text{PO}_4$ (i.e., a continuous shift of the diffraction peaks, with a narrow distribution in the b lattice parameter); this is then followed by an asymmetric broadening in the diffraction peaks, reflecting a large dispersion of lattice parameters/ d -spacings. This asymmetric broadening is a deviation from the conventional two-phase reaction and is suggestive of a single-phase, nonequilibrium transformation between $\text{Li}_{0.125}\text{Fe}_{0.875}\text{Co}_{0.125}\text{PO}_4$ and $\text{LiFe}_{0.875}\text{Co}_{0.125}\text{PO}_4$ (mechanism D).

The results in Figure 2 strongly suggest that the nonequilibrium single-phase behavior (D), previously observed only at high rates, is present even under the application of a low current. The presence of Co substituted into the LiFePO_4 structure results in more particles reacting at the same time, making it easier to detect the single-phase behavior. However, there is still evidence of the nonequilibrium single-phase transition at low cycle rates even for LiFePO_4 . Interestingly, more particles react simultaneously in the first discharge and second charge compared with the first charge. This same phenomenon was also observed at high rates for LiFePO_4 , i.e., the asymmetric peak broadening (and hence the nonequilibrium limits of the solid solution) is more significant in the first discharge and subsequent cycles than in the first charge.¹² The origin of this phenomenon is not clear, but it may be related to the presence of nonequilibrium Li^+ ion concentrations within the electrolyte, particularly when the experiments are performed at high rates; simulations are required to explore this hypothesis. The introduction of disorder in the lattice via the formation of defects (particularly in the case of the Co-substituted materials) or due to the presence of residual Li ions or vacancies in the delithiated and lithiated materials, respectively, may also result in an increase in the entropy of the system and a reduction in the tendency of the system to order, promoting solid-solution behavior.

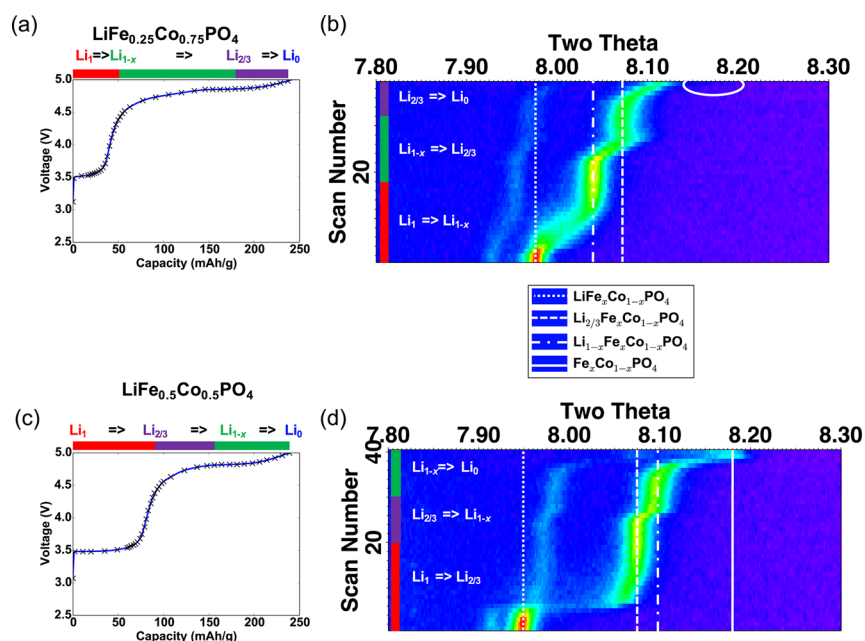


Figure 3. First-charge XRD data for (a, b) $\text{LiFe}_{0.25}\text{Co}_{0.75}\text{PO}_4$ and (c, d) $\text{LiFe}_{0.5}\text{Co}_{0.5}\text{PO}_4$ charged at a cycle rate of $C/20$. The electrochemistry collected during the in situ XRD experiments is shown by the blue solid lines in (a) and (c), and the black crosses indicate the times at which the XRD patterns were collected, i.e., when the scans commenced. The in situ XRD patterns vs scan number are shown in (b) and (d). The white lines represent the lattice parameters of the $\text{LiFe}_x\text{Co}_{1-x}\text{PO}_4$, $\text{Fe}_x\text{Co}_{1-x}\text{PO}_4$, $\text{Li}_{2/3}\text{Fe}_x\text{Co}_{1-x}\text{PO}_4$, and $\text{Li}_{1-x}\text{Fe}_x\text{Co}_{1-x}\text{PO}_4$ phases. The white ellipse indicates the calculated position of the 020 reflection for the delithiated phase, $\text{Fe}_{0.25}\text{Co}_{0.75}\text{PO}_4$, obtained using Vegard's law and the cell parameters of FePO_4 and CoPO_4 . The red, green, and purple bars alongside the figure show when the Li_{1-x} , Li_{1-x} , and $\text{Li}_{2/3}\text{Fe}_x\text{Co}_{1-x}\text{PO}_4$ phases, respectively, are being consumed in the reaction.

3.3. Highly Co-Substituted Phases. **3.3.1. $\text{LiFe}_{0.25}\text{Co}_{0.75}\text{PO}_4$ and $\text{LiFe}_{0.5}\text{Co}_{0.5}\text{PO}_4$.** The electrochemistry and in situ XRD patterns for the first charge of the highly substituted olivine material, $\text{LiFe}_{0.25}\text{Co}_{0.75}\text{PO}_4$, are shown in Figure 3a,b. In agreement with the Fe-rich materials, the intermediate, $\text{Li}_{1-x}\text{Fe}_x\text{Co}_{1-x}\text{PO}_4$, is seen at the end of the $\text{Fe}^{2+}/\text{Fe}^{3+}$ redox plateau. Interestingly, a second intermediate is also observed, which on the basis of our previous study of LiCoPO_4 , in which a $\text{Li}_{2/3}\text{CoPO}_4$ intermediate was identified, has the Li stoichiometry $\text{Li}_{2/3}\text{Fe}_x\text{Co}_{1-x}\text{PO}_4$.²⁴ Using Vegard's law and assuming a constant variation in the lattice parameters across the series $\text{Fe}_x\text{Co}_{1-x}\text{PO}_4$ ($0 \leq x \leq 1$) and $\text{Li}_y\text{Fe}_{0.25}\text{Co}_{0.75}\text{PO}_4$ ($0 \leq y \leq 1$), we can estimate the expected lattice parameters for $\text{Fe}_{0.25}\text{Co}_{0.75}\text{PO}_4$ (the resulting approximate position of the 020 reflection is shown with a white ellipse in Figure 3). Surprisingly, the reflections from $\text{Fe}_{0.25}\text{Co}_{0.75}\text{PO}_4$ are difficult to detect in Figure 3b during the first charge, despite a capacity of over 91% of the theoretical capacity (i.e., $153 \text{ mA h}^{-1} \text{ g}^{-1}$, compared with the theoretical capacity of $167.75 \text{ mA h}^{-1} \text{ g}^{-1}$) in both the first and second cycles. The fully delithiated phase is, however, more clearly seen in the second cycle (see Figure S9), and close inspection of the individual XRD patterns at the end of first charge, as shown in Figure S9, does reveal small, weak reflections at the same positions observed for $\text{Fe}_{0.25}\text{Co}_{0.75}\text{PO}_4$ in the second cycle.

The in situ XRD patterns for the first charge of $\text{LiFe}_{0.5}\text{Co}_{0.5}\text{PO}_4$ (Figure 3d) also contain reflections from two intermediate compositions in addition to those of the fully lithiated and delithiated materials. On the basis of Vegard analysis, they are assigned to Li stoichiometries of $\text{Li}_{2/3}$ and Li_{1-x} . This is in very good agreement with the first charge of the $\text{LiFe}_{0.25}\text{Co}_{0.75}\text{PO}_4$ material. Interestingly, both intermediates are formed during the $\text{Fe}^{2+}/\text{Fe}^{3+}$ plateau, with $\text{Li}_{2/3}\text{Fe}_{0.5}\text{Co}_{0.5}\text{PO}_4$ forming first, followed by $\text{Li}_{0.5}\text{Fe}_{0.5}\text{Co}_{0.5}\text{PO}_4$. The $\text{Li}_{0.5}\text{Fe}_{0.5}\text{Co}_{0.5}\text{PO}_4$ phase forms at a charge capacity of $137 \text{ mA h}^{-1} \text{ g}^{-1}$ (which is 81.3% of the theoretical capacity of $168.5 \text{ mA h}^{-1} \text{ g}^{-1}$). However, as already discussed, the

capacities of the first charge are significantly higher than the theoretical capacities as a result of side reactions, SEI formation, and/or electrolyte decomposition. Therefore, in order to determine the Li composition of this intermediate, we use (a) the unit cell volume, which by Vegard's law indicates that the phase has a stoichiometry of $\text{Li}_{0.48}$, and (b) the voltage at which the $\text{Li}_{0.5}\text{Fe}_{0.5}\text{Co}_{0.5}\text{PO}_4$ phase forms, $\sim 4.78 \text{ V}$ (i.e., after the $\text{Fe}^{2+}/\text{Fe}^{3+}$ redox plateau and before the higher-voltage $\text{Co}^{2+}/\text{Co}^{3+}$ plateau).

3.3.2. The Coherent Interface. A whole-powder-pattern fit was performed for $\text{LiFe}_{0.25}\text{Co}_{0.75}\text{PO}_4$, and the population density plot of the b lattice parameter is shown as a function of scan number in Figure 4a. The first intermediate, $\text{Li}_{0.75}\text{Fe}_{0.25}\text{Co}_{0.75}\text{PO}_4$, is formed via a two-phase reaction from the fully lithiated phase. It can be seen that $\text{LiFe}_{0.25}\text{Co}_{0.75}\text{PO}_4$ and $\text{Li}_{0.75}\text{Fe}_{0.25}\text{Co}_{0.75}\text{PO}_4$ have significant Li solubility ranges. To study this first phase transition more closely, the individual XRD patterns (in the 2θ range containing the 020 and 211 reflections) for the beginning of charge ($\text{LiFe}_{0.25}\text{Co}_{0.75}\text{PO}_4 \rightarrow \text{Li}_{0.75}\text{Fe}_{0.25}\text{Co}_{0.75}\text{PO}_4$) are shown in Figure 4b. When the $\text{Li}_{0.75}\text{Fe}_{0.25}\text{Co}_{0.75}\text{PO}_4$ phase first nucleates in the parent phase (fully lithiated $\text{LiFe}_{0.25}\text{Co}_{0.75}\text{PO}_4$ particles), the volume extends toward the volume of $\text{LiFe}_{0.25}\text{Co}_{0.75}\text{PO}_4$, which results in a shift in the XRD peak position (Figure 4b), suggesting the presence of a coherent interface between the two phases within the same particle (mechanism E in Figure 1 and Figure 4b).¹⁴ The same is observed when $\text{LiFe}_{0.25}\text{Co}_{0.75}\text{PO}_4$ is the minority phase in the $\text{Li}_{0.75}\text{Fe}_{0.25}\text{Co}_{0.75}\text{PO}_4$ particle.

The distortion in the crystal structure of the minority phase as it nucleates in the majority phase arises from the structural elasticity in the minority phase, which allows it to be accommodated in the majority phase of the particle while reducing the energy at the interface of the two phases. Hence, there is both a change in intensity in the Bragg diffraction peaks (as the nucleating phase grows at the expense of the parent phase) and a shift in the peak

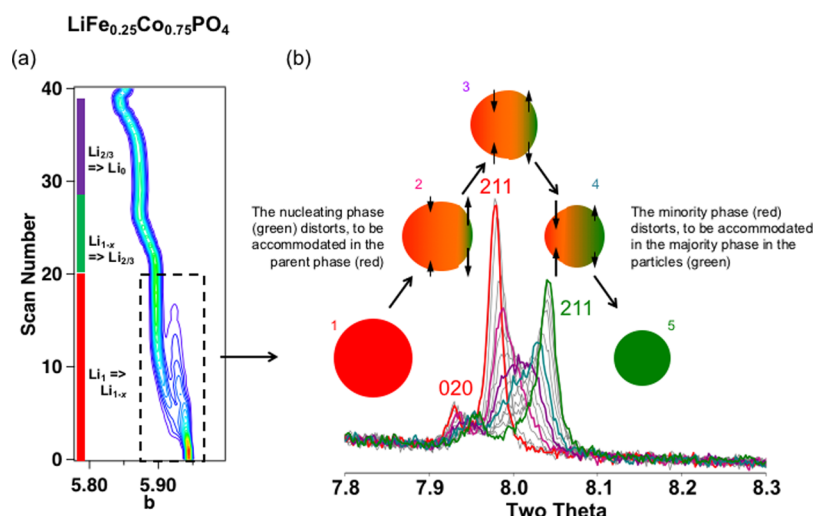


Figure 4. (a) Variations of the b lattice parameter of $\text{LiFe}_{0.25}\text{Co}_{0.75}\text{PO}_4$, plotted as the population density, as a function of the scan number, extracted from refinements using whole-powder-pattern fits. (b) XRD patterns of the phase transition from $\text{LiFe}_{0.25}\text{Co}_{0.75}\text{PO}_4$ to $\text{Li}_{0.75}\text{Fe}_{0.25}\text{Co}_{0.75}\text{PO}_4$ (i.e., scan numbers 0–20, the region highlighted by the black dashed line in (a)). The XRD response is characteristic of a coherently nucleating phase (i.e., $\text{Li}_{0.75}\text{Fe}_{0.25}\text{Co}_{0.75}\text{PO}_4$, represented in green) in the parent-phase particle (where red represents $\text{LiFe}_{0.25}\text{Co}_{0.75}\text{PO}_4$). The five cartoons labeled 1–5 represent the states of transforming particles at times corresponding to the red, pink, purple, teal, and green diffraction patterns (at capacities of 0, 37, 80, 103, and 115 $\text{mA h}^{-1} \text{g}^{-1}$, respectively, representing scan numbers 1, 5, 8, 10, and 15, respectively). The red, green, and purple bars alongside the figure indicate when the Li_1 , Li_{1-x} , and $\text{Li}_{2/3}\text{Fe}_x\text{Co}_{1-x}\text{PO}_4$ phases, respectively, are being consumed in the reaction.

positions due to the structural distortions. This phenomenon is observed to a degree in all of the two-phase reactions but is much more pronounced in phase transformations of the highly substituted samples; it was nonetheless clearly visible in the LiCoPO_4 to $\text{Li}_{2/3}\text{CoPO}_4$ reaction.²⁴

XRD peak profile simulations were carried out on 100 nm cubic $\text{LiFe}_{0.25}\text{Co}_{0.75}\text{PO}_4$ particles. Two-phase reactions between $\text{LiFe}_{0.25}\text{Co}_{0.75}\text{PO}_4$ and $\text{Li}_{0.75}\text{Fe}_{0.25}\text{Co}_{0.75}\text{PO}_4$, between $\text{Li}_{0.75}\text{Fe}_{0.25}\text{Co}_{0.75}\text{PO}_4$ and $\text{Li}_{2/3}\text{Fe}_{0.25}\text{Co}_{0.75}\text{PO}_4$, and between $\text{Li}_{2/3}\text{Fe}_{0.25}\text{Co}_{0.75}\text{PO}_4$ and $\text{Fe}_{0.25}\text{Co}_{0.75}\text{PO}_4$ were modeled with a coherent interface ranging between 5 and 200 nm in length as described in section 2.5. The length of the interface is the quantity L that appears in eq 7, which describes a concentration profile along the a axis of the particle. When the length of the interface approaches or becomes greater than the size of the particle (100 nm), the concentration gradient spans across the entire particle, which does not have two well-defined phases and appears more like a single-phase solid solution. (Representative concentration profiles are illustrated in Figure S10.) It should be noted that when the coherent interface is 200 nm in size, the peaks continually and gradually shift from the reactants to the products, i.e., the response approaches that expected for a bulk single-phase mechanism (scheme C). The results for the evolution of the 020 XRD peak are shown in Figure 5. There is reasonable agreement between the simulation and the experimental data of the coherent interface: the peaks of the minority phase distort significantly toward the values of the majority phase (Figure 5c). The simulations suggest that the $\text{LiFe}_{0.25}\text{Co}_{0.75}\text{PO}_4 \rightarrow \text{Li}_{1-x}\text{Fe}_x\text{Co}_{1-x}\text{PO}_4$ reaction proceeds via the two-phase mechanism with a coherent interface for which $60 < L < 100$ nm. In contrast, the $\text{Li}_{1-x}\text{Fe}_x\text{Co}_{1-x}\text{PO}_4 \rightarrow \text{Li}_{2/3}\text{Fe}_x\text{Co}_{1-x}\text{PO}_4$ and $\text{Li}_{2/3}\text{Fe}_x\text{Co}_{1-x}\text{PO}_4 \rightarrow \text{Fe}_x\text{Co}_{1-x}\text{PO}_4$ reactions both show continuous and gradual shifts in the XRD peaks, corresponding to the two-phase mechanism with a coherent interface for which $L = 200$ nm, i.e., the bulk solid-solution mechanism.

It should be noted that we have assumed the nucleating phase growing within the majority component has the same composition

and thus cell parameters as the bulk phase, with the composition varying across the interface. It is also important to emphasize that more than one coherent interface may exist in one particle simultaneously.

3.3.3. Systematic Analysis of Cell Parameter Changes. The same analysis as described in section 3.3.1 for $\text{LiFe}_{0.25}\text{Co}_{0.75}\text{PO}_4$ and $\text{LiFe}_{0.5}\text{Co}_{0.5}\text{PO}_4$ was carried out for all of the other $\text{LiFe}_x\text{Co}_{1-x}\text{PO}_4$ phases ($x = 1, 0.95, 0.875, 0.75, 0.125, 0.05, 0$). The cell parameters for the intermediates and end-member phases for all nine ratios were extracted from Rietveld refinements of the XRD patterns (all of the raw data is shown in Figure S11). The unit cell volumes of the end members and intermediates extracted from the Rietveld refinements of the XRD patterns are plotted against Fe content (x) in Figure 6. The phases corresponding to $\text{LiFe}_x\text{Co}_{1-x}\text{PO}_4$, $\text{Li}_{1-x}\text{Fe}_x\text{Co}_{1-x}\text{PO}_4$, $\text{Li}_{2/3}\text{Fe}_x\text{Co}_{1-x}\text{PO}_4$, and $\text{Fe}_x\text{Co}_{1-x}\text{PO}_4$ are shown by red, green, purple, and blue data points, respectively. There is a linear increase in the volume of $\text{LiFe}_x\text{Co}_{1-x}\text{PO}_4$ (shown in red) with increasing x . This is in agreement with the literature^{41,42} and is a result of the homogeneous mixing of the transition metals in the olivine structure (assuming that Vegard's law applies). Similarly, the a and b lattice parameters (shown in Figure S12) increase with increasing Fe content because of the larger ionic radius of Fe^{2+} compared with Co^{2+} (92 and 88.5 pm, respectively, assuming a high-spin ion in an octahedral environment).⁴³ Interestingly, the c axis decreases with increasing Fe content, and although the origin for this behavior is unknown, it is thought to be related to the stiffness of the P–O bonds (effectively rigid PO_4 tetrahedra) and the shared edges between the PO_4 and MO_6 polyhedra,⁴¹ with the phosphate ions acting to separate or pillar the chains of edge-sharing MO_6 octahedra. The changes in the volume for $\text{Fe}_x\text{Co}_{1-x}\text{PO}_4$ (blue dashed line) display the same linear gradient as those for the lithiated phases, presumably because the difference in Co and Fe cation sizes is identical for the divalent and trivalent cations. The volume of the $\text{Li}_{2/3}\text{Fe}_x\text{Co}_{1-x}\text{PO}_4$ intermediate (observed for the Co-majority materials, $0 \leq x \leq 0.5$) lies two-thirds of the way between those of the fully lithiated and delithiated phases

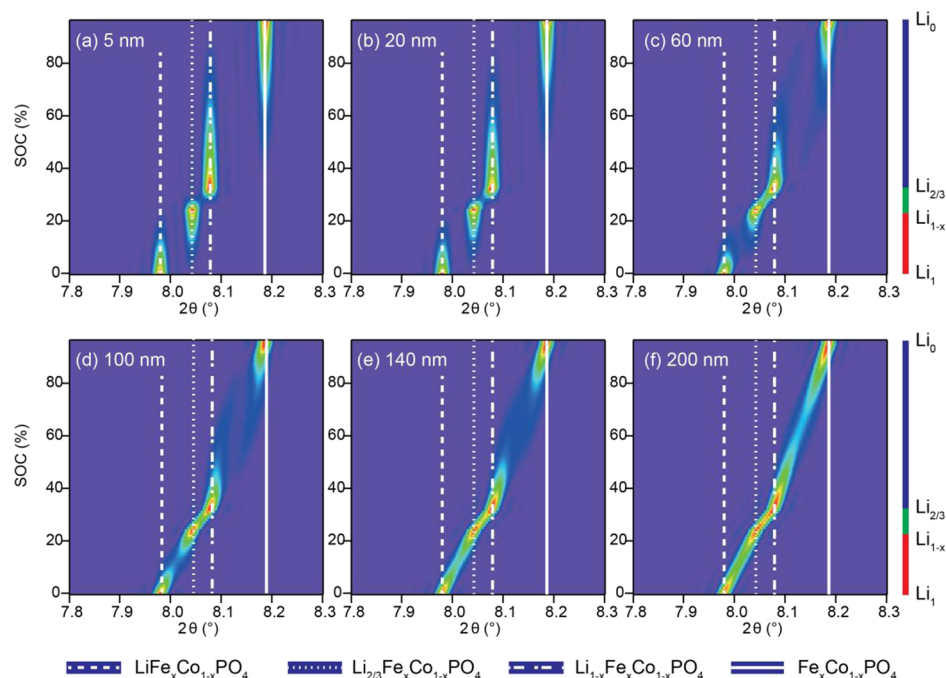


Figure 5. Simulations of the evolution of 020 XRD peak profiles for a two-phase reaction with a coherent interface between $\text{LiFe}_{0.25}\text{Co}_{0.75}\text{PO}_4$ and $\text{Li}_{0.75}\text{Fe}_{0.25}\text{Co}_{0.75}\text{PO}_4$, between $\text{Li}_{0.75}\text{Fe}_{0.25}\text{Co}_{0.75}\text{PO}_4$ and $\text{Li}_{2/3}\text{Fe}_{0.25}\text{Co}_{0.75}\text{PO}_4$, and between $\text{Li}_{2/3}\text{Fe}_{0.25}\text{Co}_{0.75}\text{PO}_4$ and $\text{Fe}_{0.25}\text{Co}_{0.75}\text{PO}_4$ in 100 nm sized cubic $\text{LiFe}_{0.25}\text{Co}_{0.75}\text{PO}_4$ particles, assuming that the interface is (a) 5 nm, (b) 20 nm, (c) 60 nm, (d) 100 nm, (e) 140 nm, and (f) 200 nm in size at different states of charge (SOC). The red, green, and purple bars alongside the figure show when the Li_{1-} , Li_{1-x} , and $\text{Li}_{2/3}\text{Fe}_x\text{Co}_{1-x}\text{PO}_4$ phases, respectively, are being consumed in the reaction.

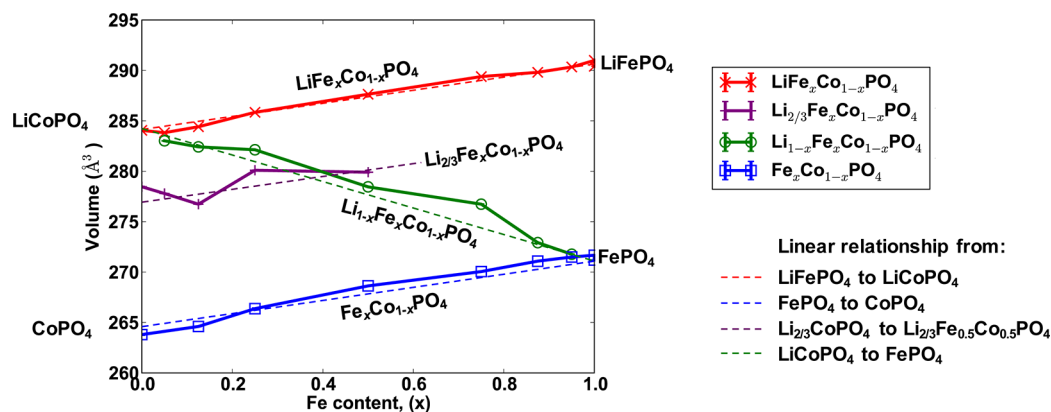


Figure 6. Unit cell volumes of the end-member and intermediate phases observed when $\text{LiFe}_x\text{Co}_{1-x}\text{PO}_4$ is delithiated. The red dashed line represents linear volume changes in going from LiFePO_4 to LiCoPO_4 calculated using the end-member volumes. The same gradient as used for the lithiated phases (red) was used for the delithiated and $\text{Li}_{2/3}\text{Fe}_x\text{Co}_{1-x}\text{PO}_4$ materials (blue and purple dashed lines, respectively). The blue line was drawn to go through the delithiated unit cell volume data, and the purple line was placed two-thirds of the way between the delithiated and lithiated data (i.e., it is not a fit to the data). The green dashed line simply connects the experimental cell volumes of LiCoPO_4 and FePO_4 .

(purple dashed line), and the volume of the $\text{Li}_{1-x}\text{Fe}_x\text{Co}_{1-x}\text{PO}_4$ intermediates varies linearly between those of LiCoPO_4 and FePO_4 with increasing Fe content (green dashed line). This simple analysis using Vegard's rule is in good agreement with the Li stoichiometries assigned to the intermediates observed during the first charge of $\text{LiFe}_x\text{Co}_{1-x}\text{PO}_4$ ($x = 0.95, 0.875, 0.75, 0.5, 0.125, 0.05$). Although no obvious trends for the compositions and cell parameters of the different intermediates emerge when each composition is studied individually, the systematic examination of the phases as a function of Fe:Co ratio reveals clear correlations with respect to the Li composition and cell parameters of the intermediate phases.

The percentage differences in the a , b , and c axes, the ab , ac , and bc planes, and the volumes of the two intermediates and the

end-member structures relative to LiFePO_4 have been calculated and are shown in Figure S13. As was observed in the $\text{LiFe}_x\text{Mn}_{1-x}\text{PO}_4$ materials¹⁴ and for LiCoPO_4 ,²⁴ there is a very small difference (<2%) in the bc plane among all of the structures. This strongly suggests that when there is a coherent interface, it is likely to be in this plane, resulting in the lowest size mismatch and therefore the lowest strain compared with interfaces along the ab and bc planes. This arises from the contraction of the c axis with both increasing Co content and decreasing Li content from LiFePO_4 and the smaller expansion along the b axis compared with the a axis. We now consider separately how the delithiation mechanisms vary among the starting, intermediate, and end-member phases, comparing the mechanisms as a function of Co content.

3.4. $\text{LiFe}_x\text{Co}_{1-x}\text{PO}_4$ Delithiation Mechanisms upon Charging.

3.4.1. Delithiation Mechanisms between the Two Intermediates $\text{Li}_{1-x}\text{Fe}_x\text{Co}_{1-x}\text{PO}_4$ and $\text{Li}_{2/3}\text{Fe}_x\text{Co}_{1-x}\text{PO}_4$. As shown in Figure 6, when the four substituted olivines $\text{LiFe}_{0.05}\text{Co}_{0.95}\text{PO}_4$, $\text{LiFe}_{0.125}\text{Co}_{0.875}\text{PO}_4$, $\text{LiFe}_{0.25}\text{Co}_{0.75}\text{PO}_4$, and $\text{LiFe}_{0.5}\text{Co}_{0.5}\text{PO}_4$ are delithiated, two intermediates are observed, $\text{Li}_{1-x}\text{Fe}_x\text{Co}_{1-x}\text{PO}_4$ and $\text{Li}_{2/3}\text{Fe}_x\text{Co}_{1-x}\text{PO}_4$. We now investigate in more detail how the structural transformation between these two intermediate phases occurs. We start with this transformation because it is the simplest mechanism observed in this system. A whole-powder-pattern fit was performed for all four materials during the delithiation between the two intermediates, and the population density plots of the b lattice parameter as a function of scan number are shown in Figure 7 (for clarity, only the b lattice parameter changes are shown here; the a , b , and c lattice parameter changes can be found in Figures S14–S16). The decrease in the intensity of the lattice parameter population densities for $\text{LiFe}_{0.05}\text{Co}_{0.95}\text{PO}_4$ is attributed to the loss of long-range order, similar to that observed upon charging of LiCoPO_4 . For the three higher-Fe-content materials, continuous intensity connecting the lattice parameters of the $\text{Li}_{1-x}\text{Fe}_x\text{Co}_{1-x}\text{PO}_4$ and $\text{Li}_{2/3}\text{Fe}_x\text{Co}_{1-x}\text{PO}_4$ phases is observed, providing evidence for a bulk single-phase transformation (mechanism C). This is noticeably different from the response in the lattice parameters observed for both the discrete nonequilibrium single-phase mechanism (D) and the two-phase mechanism exhibiting a large coherent interface (shown in Figure 4b, mechanism E).

The single-phase mechanism between the intermediates appears to be preferred because of the disorder of the transition metals on the Fe/Co sublattice. The homogeneous mixing of Fe^{2+} and Co^{2+} on the transition metal sublattice in the starting

materials⁴² results in a random distribution of Fe^{3+} and Co^{2+} in the $\text{Li}_{1-x}(\text{Fe}^{3+})_x(\text{Co}^{2+})_{1-x}\text{PO}_4$ intermediate. Unless there is an energy gain for Li^+ /vacancy ordering, this also results in a random distribution of Li^+ ions in the particles, with Li^+ preferentially occupying sites close to Co^{2+} (or more generally M^{2+}) because of the reduction in Li^+ –transition metal cation repulsive Coulombic interactions arising from the lower charge of Co^{2+} versus Fe^{3+} . The existence of a distribution of Li^+ /vacancies and $\text{Fe}^{3+}/\text{Co}^{2+}$ in the $\text{Li}_{1-x}\text{Fe}_x\text{Co}_{1-x}\text{PO}_4$ intermediate helps favor the bulk single-phase mechanism for the $\text{Co}^{2+}/\text{Co}^{3+}$ process for $\text{LiFe}_{0.05}\text{Co}_{0.95}\text{PO}_4$, $\text{LiFe}_{0.125}\text{Co}_{0.875}\text{PO}_4$, and $\text{LiFe}_{0.25}\text{Co}_{0.75}\text{PO}_4$. As discussed in section 3.3.1, the $\text{Li}_{2/3}$ intermediate is also formed on the $\text{Fe}^{2+}/\text{Fe}^{3+}$ oxidation plateau for $\text{LiFe}_{0.5}\text{Co}_{0.5}\text{PO}_4$, which means that this single-phase mechanism also occurs between the intermediates during Fe^{2+} oxidation. Therefore, it is likely that the single-phase mechanism between the intermediates is also preferred because of the small change in volume between $\text{Li}_{2/3}\text{Fe}_x\text{Co}_{1-x}\text{PO}_4$ and $\text{Li}_{1-x}\text{Fe}_x\text{Co}_{1-x}\text{PO}_4$ (see the plot at the bottom of Figure 7).

3.4.2. Delithiation Mechanisms To Form the Fully Delithiated Phase, $\text{Fe}_x\text{Co}_{1-x}\text{PO}_4$. We now examine the mechanisms that occur to form $\text{Fe}_x\text{Co}_{1-x}\text{PO}_4$ at the end of the first charge. A whole-powder-pattern fit was performed for $\text{LiFe}_{0.875}\text{Co}_{0.125}\text{PO}_4$, $\text{LiFe}_{0.75}\text{Co}_{0.25}\text{PO}_4$, $\text{LiFe}_{0.5}\text{Co}_{0.5}\text{PO}_4$, and $\text{LiFe}_{0.125}\text{Co}_{0.875}\text{PO}_4$, and the population density plots of the b lattice parameter as a function of scan number in the region of the charge profile when the fully delithiated phase forms are shown in Figure 8. For the Fe-rich samples, this represents the transformation from $\text{Li}_{1-x}\text{Fe}_x\text{Co}_{1-x}\text{PO}_4$ to $\text{Fe}_x\text{Co}_{1-x}\text{PO}_4$, while for the higher-Co-content sample ($\text{LiFe}_{0.125}\text{Co}_{0.875}\text{PO}_4$) this corresponds to a transition from the $\text{Li}_{2/3}\text{Fe}_x\text{Co}_{1-x}\text{PO}_4$ phase. Three samples were not included in this

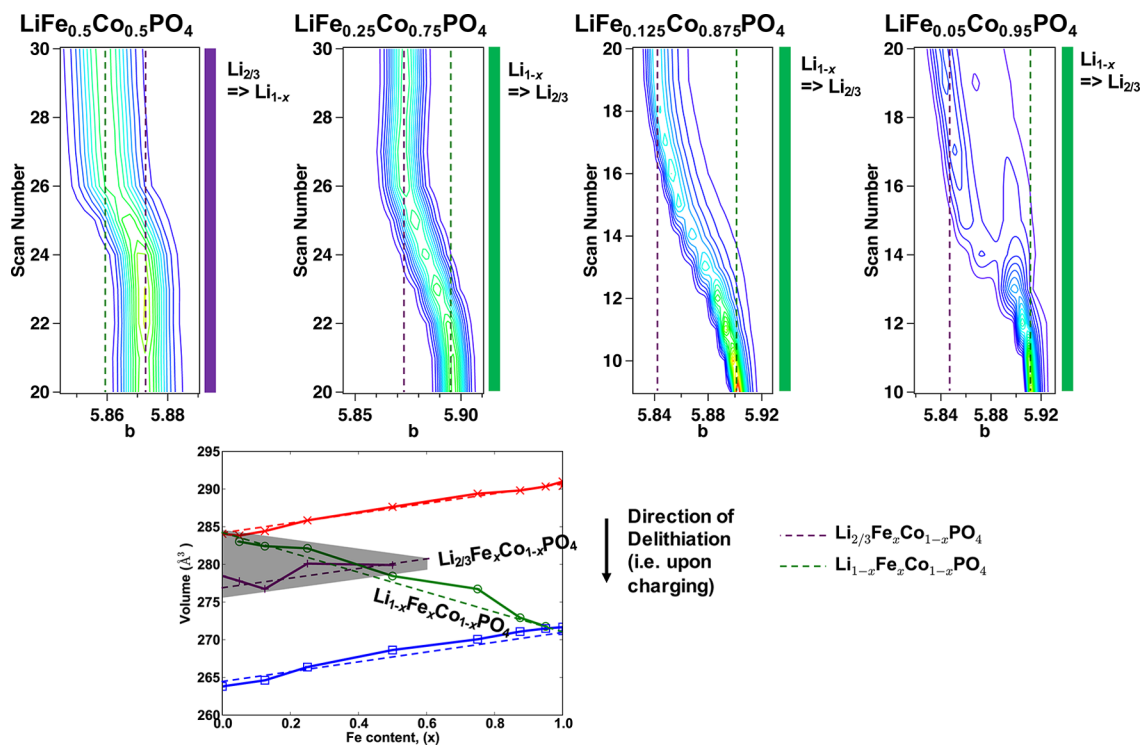


Figure 7. Variations in the b lattice parameter, plotted as population density, as a function of the scan number for $\text{LiFe}_{0.5}\text{Co}_{0.5}\text{PO}_4$, $\text{LiFe}_{0.25}\text{Co}_{0.75}\text{PO}_4$, $\text{LiFe}_{0.125}\text{Co}_{0.875}\text{PO}_4$, and $\text{LiFe}_{0.05}\text{Co}_{0.95}\text{PO}_4$. These were extracted from refinements using whole-powder-pattern fits. The plot at the bottom shows the volume changes between the intermediate phases. The gray-shaded area indicates the phases being investigated in this section and whose cell parameters are shown in this figure. The green and purple bars alongside the plots indicate when the Li_{1-x} and $\text{Li}_{2/3}\text{Fe}_x\text{Co}_{1-x}\text{PO}_4$ phases, respectively, are being consumed in the reaction.

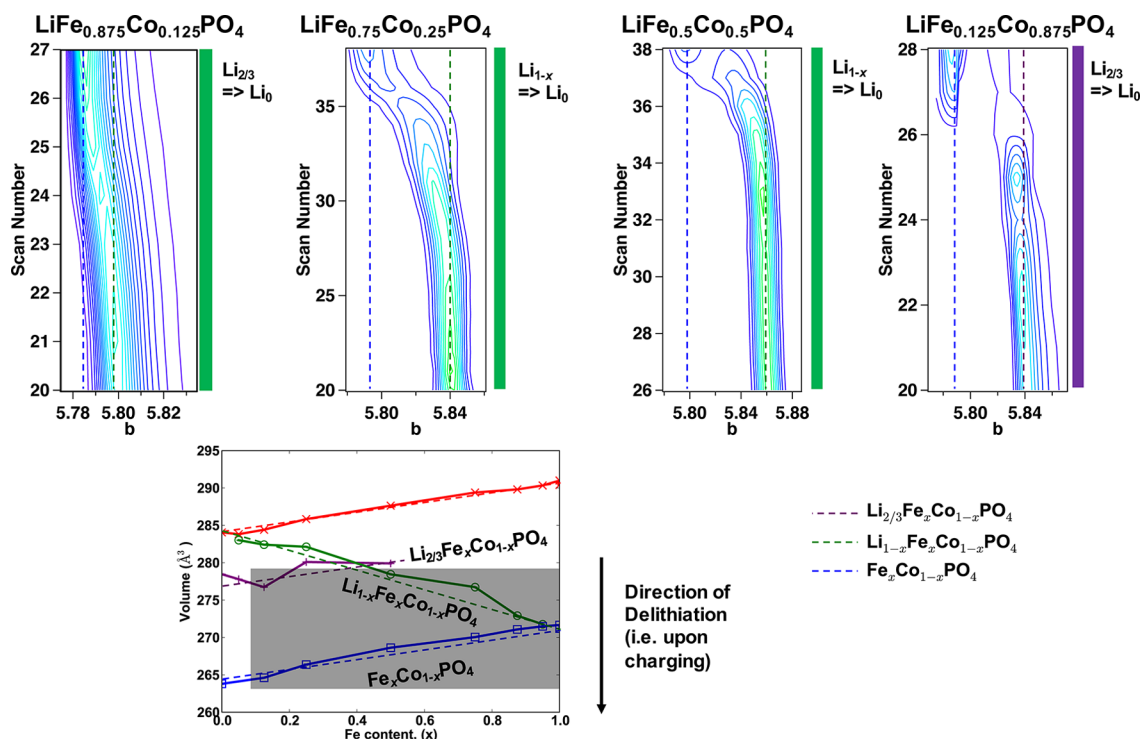


Figure 8. Variations in the b lattice parameter, plotted as population density, as a function of the scan number for $\text{LiFe}_{0.875}\text{Co}_{0.125}\text{PO}_4$, $\text{LiFe}_{0.75}\text{Co}_{0.25}\text{PO}_4$, $\text{LiFe}_{0.5}\text{Co}_{0.5}\text{PO}_4$, and $\text{LiFe}_{0.125}\text{Co}_{0.875}\text{PO}_4$. These were extracted from refinements using whole-powder-pattern fits. The plot at the bottom shows the volume changes as a function of Fe content, and the gray-shaded region indicates the phase changes being investigated in this figure. The green and purple bars alongside the plots show when the Li_{1-x} and $\text{Li}_{2/3}\text{Fe}_x\text{Co}_{1-x}\text{PO}_4$ phases, respectively, are being consumed in the reaction.

analysis because the fully delithiated phase was not clearly observed on the first charge ($\text{LiFe}_{0.25}\text{Co}_{0.75}\text{PO}_4$; see section 3.3.1), no XRD patterns were obtained for the full charge (for $\text{LiFe}_{0.05}\text{Co}_{0.95}\text{PO}_4$) because of time limitations at the synchrotron, and for LiCoPO_4 the significant loss of long-range order results in reduced intensity of the Bragg reflections, making the data difficult to interpret using this method of analysis.

When $\text{LiFe}_{0.875}\text{Co}_{0.125}\text{PO}_4$ is fully delithiated, there is a continuous and gradual shift in the lattice parameters from the $\text{Li}_{0.125}\text{Fe}_{0.875}\text{Co}_{0.125}\text{PO}_4$ phase to $\text{Fe}_{0.875}\text{Co}_{0.125}\text{PO}_4$, indicating that the bulk single-phase mechanism (scheme C) is observed. As discussed in section 3.4.1, the single-phase mechanism is preferred because of (i) the disorder of Li^+ /vacancies and $\text{Fe}^{3+}/\text{Co}^{2+}$ in $\text{Li}_{1-x}\text{Fe}_x\text{Co}_{1-x}\text{PO}_4$, which helps favor the single-phase mechanism during the oxidation of Co^{2+} , and (ii) the small change in volume. For both $\text{LiFe}_{0.75}\text{Co}_{0.25}\text{PO}_4$ and $\text{LiFe}_{0.5}\text{Co}_{0.5}\text{PO}_4$, single-phase behavior is also observed upon delithiation of $\text{Li}_{1-x}\text{Fe}_x\text{Co}_{1-x}\text{PO}_4$, but fewer particles appear to react at once compared with $\text{LiFe}_{0.875}\text{Co}_{0.125}\text{PO}_4$ (i.e., the number of reacting particles decreases with decreasing Fe content in going from $\text{LiFe}_{0.875}\text{Co}_{0.125}\text{PO}_4$ to $\text{LiFe}_{0.75}\text{Co}_{0.25}\text{PO}_4$ to $\text{LiFe}_{0.5}\text{Co}_{0.5}\text{PO}_4$). A continuous shift in the lattice parameters can be seen in going from $\text{Li}_{1-x}\text{Fe}_{0.75}\text{Co}_{0.25}\text{PO}_4$ to $\text{Fe}_{0.75}\text{Co}_{0.25}\text{PO}_4$, whereas for the $\text{Li}_{0.5}\text{Fe}_{0.5}\text{Co}_{0.5}\text{PO}_4 \rightarrow \text{Fe}_{0.5}\text{Co}_{0.5}\text{PO}_4$ reaction significant asymmetric deviations of the end-member phases toward each other are observed. This implies that the single-phase mechanism is to a degree occurring discretely between particles (scheme D) rather than simultaneously (i.e., at the bulk level, scheme C). This change from particles reacting discretely compared with simultaneously is even more pronounced during the reaction of $\text{Li}_{2/3}\text{Fe}_{0.125}\text{Co}_{0.875}\text{PO}_4$ to form $\text{Fe}_{0.125}\text{Co}_{0.875}\text{PO}_4$.

To summarize, during the oxidation of Co^{2+} to Co^{3+} , a single-phase (solid-solution) mechanism occurs within individual particles to form fully delithiated $\text{Fe}_x\text{Co}_{1-x}\text{PO}_4$. At low levels of Fe substitution (i.e., $\text{LiFe}_{0.125}\text{Co}_{0.875}\text{PO}_4$), the reaction occurs discretely, particle-by-particle. As the level of Fe substitution increases, more particles react simultaneously, resulting in increasingly more bulk single-phase-like behavior. At high Fe contents, i.e., $\text{LiFe}_{0.875}\text{Co}_{0.125}\text{PO}_4$, essentially ideal single-phase behavior is observed.

3.4.3. Delithiation Mechanisms Occurring during the Reaction of Fully Lithiated $\text{LiFe}_x\text{Co}_{1-x}\text{PO}_4$. Finally, we examine the first delithiation reaction that occurs upon charging of $\text{LiFe}_x\text{Co}_{1-x}\text{PO}_4$ for $x = 1, 0.95, 0.875, 0.75, 0.5, 0.25, 0.125$, and 0.05. A whole-powder-pattern fit was performed for all eight of the materials, and the population density plots of the b lattice parameter as a function of scan number are shown in Figure 9 for the initial delithiation of the pristine $\text{LiFe}_x\text{Co}_{1-x}\text{PO}_4$ phase. LiCoPO_4 is not included since we focus here on the mechanism that occurs on the $\text{Fe}^{2+}/\text{Fe}^{3+}$ oxidation plateau.

As discussed in section 3.2, the delithiation of the Fe-rich materials (LiFePO_4 , $\text{LiFe}_{0.95}\text{Co}_{0.05}\text{PO}_4$, and $\text{LiFe}_{0.875}\text{Co}_{0.125}\text{PO}_4$) appears to occur via a simple “two-phase” reaction (as only the two end-member phases are observed, as depicted in mechanism B). However, further analysis of the first discharge and second charge reveals that the transformation between the two phases (between LiFePO_4 and FePO_4 and between $\text{LiFe}_x\text{Co}_{1-x}\text{PO}_4$ and $\text{Li}_{1-x}\text{Fe}_x\text{Co}_{1-x}\text{PO}_4$ for $x = 0.95$ and 0.875) occurs via the non-equilibrium single-phase mechanism (D). Since very few particles react at once, the two end-member phases dominate the response. As the Co-substitution level increases (from 0 to 0.05 to 0.125), more particles react at once and the asymmetric deviations from

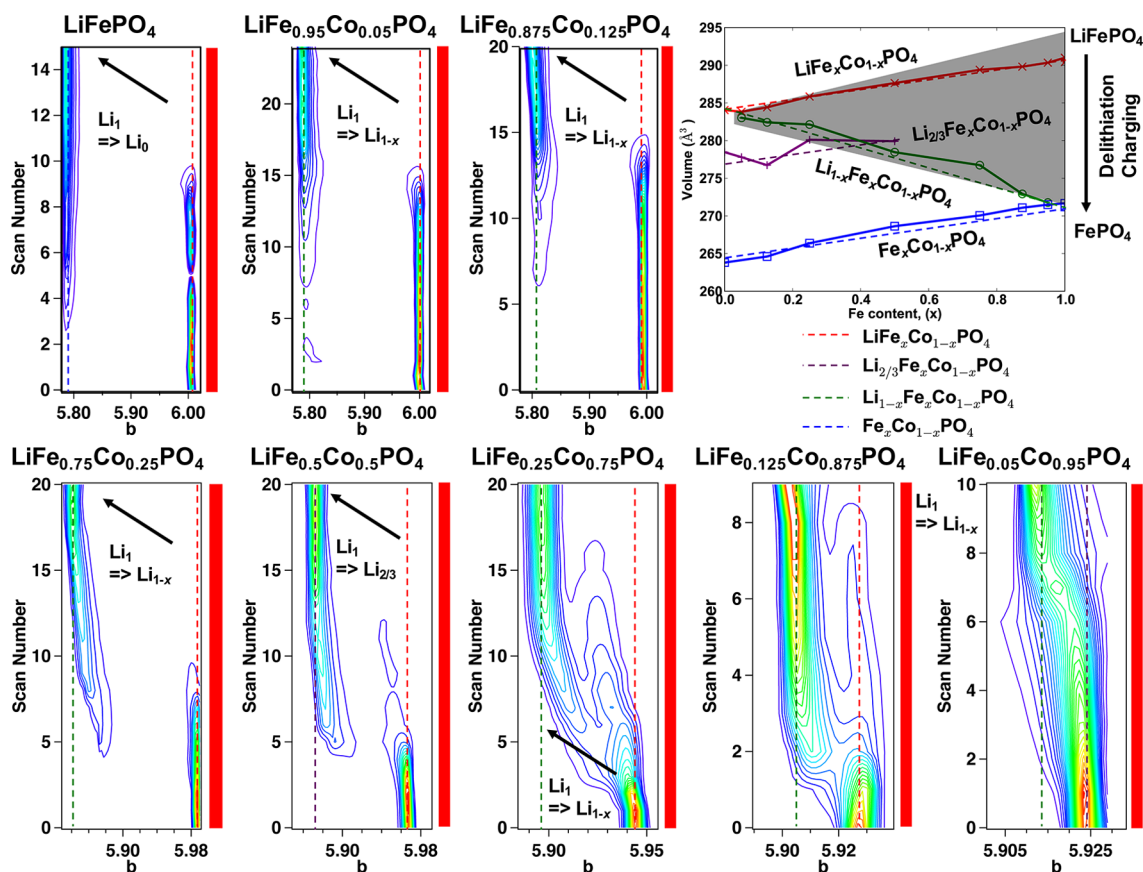


Figure 9. Variations in the b lattice parameter, plotted as population density, as a function of the scan number for $\text{LiFe}_x\text{Co}_{1-x}\text{PO}_4$ with $x = 1, 0.95, 0.875, 0.75, 0.5, 0.25, 0.125,$ and 0.05 . These were extracted from refinements using whole-powder-pattern fits. The plot at the top right shows the volume changes, and the gray-shaded area highlights those that occur when the fully lithiated phase is delithiated. The red bars alongside the plots indicate that it is the $\text{LiFe}_x\text{Co}_{1-x}\text{PO}_4$ phase that is being consumed as the material is delithiated.

the end-member phases toward each other are more discernible, even in the first charge (Figure 9 for $\text{LiFe}_{0.875}\text{Co}_{0.125}\text{PO}_4$).

The delithiation mechanisms for $\text{LiFe}_{0.75}\text{Co}_{0.25}\text{PO}_4$ and $\text{LiFe}_{0.5}\text{Co}_{0.5}\text{PO}_4$ at the onset of charge involve a bulk shift of the lattice parameters from those of the end members, $\text{LiFe}_x\text{Co}_{1-x}\text{PO}_4$ and $\text{Li}_{1-x}\text{Fe}_x\text{Co}_{1-x}\text{PO}_4$, as well as an asymmetric broadening in the parameters toward each other. In section 3.3, we ascribed the behavior seen for the delithiation of $\text{LiFe}_{0.25}\text{Co}_{0.75}\text{PO}_4$ to form $\text{Li}_{0.75}\text{Fe}_{0.25}\text{Co}_{0.75}\text{PO}_4$ to that of a two-phase reaction occurring in the presence of a coherent interface. Therefore, the behavior of $\text{LiFe}_{0.75}\text{Co}_{0.25}\text{PO}_4$ and $\text{LiFe}_{0.5}\text{Co}_{0.5}\text{PO}_4$ is likely to be intermediate between those of the Fe-rich materials and $\text{LiFe}_{0.25}\text{Co}_{0.75}\text{PO}_4$. We will discuss in more detail how these mechanisms are related in section 3.5.

$\text{LiFe}_{0.05}\text{Co}_{0.95}\text{PO}_4$ reacts via a bulk single-phase mechanism (mechanism C) to form the $\text{Li}_{0.95}\text{Fe}_{0.05}\text{Co}_{0.95}\text{PO}_4$ intermediate, as shown by a continuous shift in the lattice parameters, whereas $\text{LiFe}_{0.125}\text{Co}_{0.875}\text{PO}_4$ has more “two-phase”-like behavior, as shown by the coexistence of the $\text{LiFe}_{0.125}\text{Co}_{0.875}\text{PO}_4$ and $\text{Li}_{0.875}\text{Fe}_{0.125}\text{Co}_{0.875}\text{PO}_4$ lattice parameters, with some shift in the parameters toward each other. As the Fe content decreases, two phenomena occur: the difference between the cell parameters of $\text{LiFe}_x\text{Co}_{1-x}\text{PO}_4$ and $\text{Li}_{1-x}\text{Fe}_x\text{Co}_{1-x}\text{PO}_4$ decreases and the substitution levels (i.e., the disruption in the lattice) decrease. The former favors the single-phase mechanism (as observed for $\text{LiFe}_{0.05}\text{Co}_{0.95}\text{PO}_4$) and the latter results in a shorter coherent interface (as the lattice has fewer dopant Fe particles, leading to reduced structural elasticity) in the two-phase reaction, as seen

for $\text{LiFe}_{0.125}\text{Co}_{0.875}\text{PO}_4$. These two competing phenomena must cause the apparent “break” in trend for $\text{LiFe}_{0.125}\text{Co}_{0.875}\text{PO}_4$.

3.5. Discussion of How the Mechanisms Are Related and Interconvert. As demonstrated in section 3.4, there is not a sharp cutoff between the various mechanisms as the Co content increases. In Figure 10 we summarize how the mechanisms are interconnected. From previous studies^{3,6} of partially charged samples of LiFePO_4 , we know that as we increase the particle size, the two end-member phases (i.e., FePO_4 and LiFePO_4) are able to coexist within a particle rather than existing in separate particles (the transition from scheme B to scheme A in Figure 10).

We saw in section 3.2 that at low cycle rates, nanoparticulate LiFePO_4 delithiates via the single-phase mechanism with few particles reacting at once (scheme B). As the Co content increases in going from LiFePO_4 to $\text{LiFe}_{0.95}\text{Co}_{0.05}\text{PO}_4$ and $\text{LiFe}_{0.875}\text{Co}_{0.125}\text{PO}_4$, more particles react simultaneously during delithiation of the fully lithiated phase on the plateau of the $\text{Fe}^{2+}/\text{Fe}^{3+}$ oxidation reaction, as demonstrated by the pathway from scheme B to scheme D in Figure 10. The studies by Liu et al.¹² showed that as the current applied to the system increases, the same trend is observed (scheme B to scheme D). A more pronounced effect (i.e., even more particles react simultaneously) is seen when forming the fully delithiated phase during the $\text{Co}^{2+}/\text{Co}^{3+}$ oxidation reaction for increasing Fe content, for $x = 0.125, 0.5, 0.75,$ and 0.875 (scheme D to scheme C), eventually leading to the bulk single-phase mechanism (C) for the transformation between $\text{Li}_{0.125}\text{Fe}_{0.875}\text{Co}_{0.125}\text{PO}_4$ and $\text{Fe}_{0.875}\text{Co}_{0.125}\text{PO}_4$.

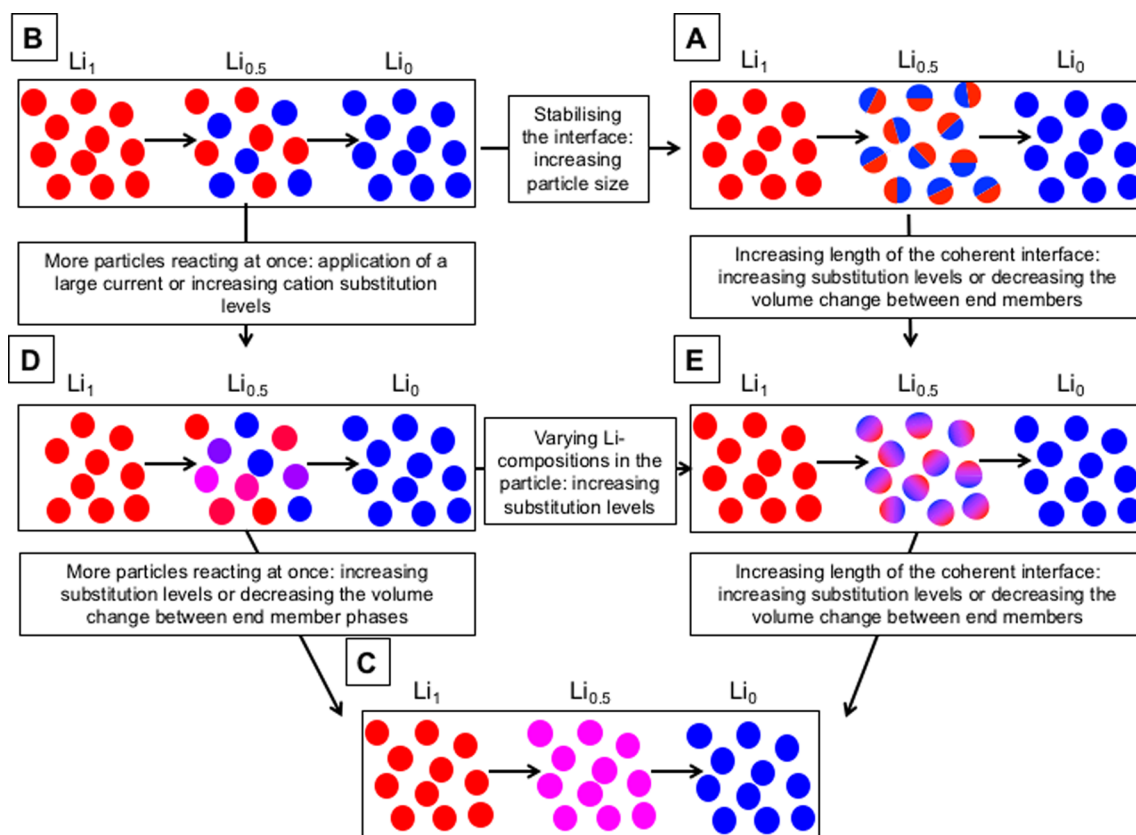


Figure 10. Schematic illustration showing how the apparently different delithiation mechanisms are interconnected. The lettering A–E corresponds to that introduced in Figure 1.

Using Figure 10, we are now able to better understand the trend in the mechanisms observed in Figure 9. We know that increasing the Co content in the substituted olivines increases the number of particles that react simultaneously during the plateau of the $\text{Fe}^{2+}/\text{Fe}^{3+}$ oxidation reaction (scheme B \rightarrow scheme D), and we know that a two-phase mechanism containing a coherent interface is observed when $\text{LiFe}_{0.25}\text{Co}_{0.75}\text{PO}_4$ is delithiated to form $\text{Li}_{0.75}\text{Fe}_{0.25}\text{Co}_{0.75}\text{PO}_4$ (scheme E). Therefore, between $\text{LiFe}_{0.75}\text{Co}_{0.25}\text{PO}_4$ and $\text{LiFe}_{0.5}\text{Co}_{0.5}\text{PO}_4$, the mechanism is transitioning from D to E: both more particles are reacting at once and the intermediate lithium compositions are now able to coexist within a particle rather than between particles. As we further increase the Co content in going from $\text{LiFe}_{0.25}\text{Co}_{0.75}\text{PO}_4$ to $\text{LiFe}_{0.05}\text{Co}_{0.95}\text{PO}_4$, we move from scheme E to scheme C: the length of the coherent interface increases to the size of the particles (as demonstrated in our simulations in Figure 5). As explained in section 3.4.3, the apparent “anomaly” in the mechanisms for $\text{LiFe}_{0.125}\text{Co}_{0.875}\text{PO}_4$ is due to opposing effects arising from the decrease in the change in volume during the reaction and the reduced coherency at the interface (owing to the decreasing amount of disorder resulting from reduced Co content). Therefore, even though it is possible to correlate the trends in the behavior in the mechanisms with changing substitution levels, because of the complicated interplay between lattice disruption and change in volume it is still not trivial to predict what mechanism will occur when. Nonetheless, studying the whole series has provided considerable insight into the general trends and dominant factors controlling the mechanism.

4. CONCLUSIONS

A comprehensive mechanistic study of the delithiation of the cosubstituted $\text{LiFe}_x\text{Co}_{1-x}\text{PO}_4$ materials was performed using

in situ XRD. Correlations between the seemingly different mechanisms have been discussed within the cosubstituted olivines (as summarized in Figure 11), the $\text{LiFe}_x\text{Co}_{1-x}\text{PO}_4$ series ($0 \leq x \leq 0.95$). They are distinguished by the length of the coherent interface and whether the intermediate Li compositions (i.e., those between the fully lithiated and fully delithiated values) coexist within or between the particles. Increasing the Co substitution level increases the number of observable particles reacting via the single-phase mechanism during the plateau of the $\text{Fe}^{2+}/\text{Fe}^{3+}$ oxidation reaction and vice versa (i.e., Fe substitution increases the observable number of particles reacting via the single-phase mechanism during the $\text{Co}^{2+}/\text{Co}^{3+}$ oxidation reaction). From previous studies,¹² we know that this is also the case when a larger current is applied. Increasing the substitution levels also allows intermediate Li compositions to exist within the particle rather than between particles (i.e., the coherent interface). It was also observed that the difference between the volumes of the two species in each transformation is important and that when there is a small difference in volume the single-phase reaction is likely to occur.

This study helps to establish how the solid solution mechanisms are related to the two-phase mechanism, how the mechanisms are affected by the varying length of the coherent interface, and how the different mechanisms can be distinguished using in situ XRD. It is key to understand how the battery electrode materials lithiate and delithiate in order to optimize current materials and provide a foundation for what characteristics future cathode materials should have (i.e., dopant and substituted materials). Critically, the formation of interfaces versus solid solutions during structural transformations can have implications for the fracturing of particles over multiple cycles: no energetically unfavorable interfaces are formed

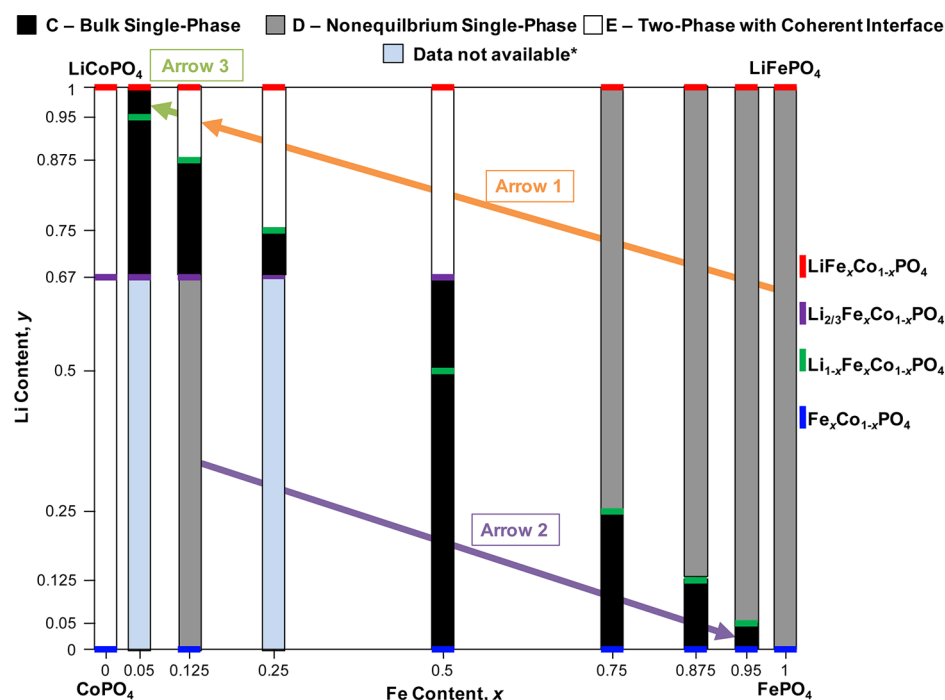


Figure 11. Pseudophase diagram of $\text{Li}_x\text{Fe}_x\text{Co}_{1-x}\text{PO}_4$ showing the evolution of the phases and the mechanisms by which they delithiate with decreasing Li content and varying Fe content ($0 \leq x, y \leq 1$). Red, green, purple, and blue represent the Li_{1-x} , Li_{1-x} , $\text{Li}_{2/3}$, and $\text{Li}_0\text{Fe}_x\text{Co}_{1-x}\text{PO}_4$ phases, respectively, and the black, gray, and white bars represent the bulk single-phase mechanism (C), the nonequilibrium single-phase mechanism occurring particle-by-particle (D), and the two-phase mechanism with a coherent interface (E), respectively. Arrow 1 shows varying Li compositions existing *within* rather than *between* the particles (scheme D to scheme E). The direction of arrow 1 shows the change of the mechanism from the single-phase transition occurring discretely between particles to the two-phase mechanism with significant coherency at the interface. The direction of arrow 2 indicates an increase in the number of particles reacting simultaneously (scheme D to scheme C). Arrow 3 shows an increasing length of the coherent interface, i.e., a transition from scheme E to scheme D. *The end of charge for $\text{LiFe}_{0.05}\text{Co}_{0.95}\text{PO}_4$ was not collected because of limitations at the beamline, and the fully delithiated phase was not observed on the first charge for $\text{LiFe}_{0.25}\text{Co}_{0.75}\text{PO}_4$.

for a solid solution, leading to improved capacity retention. Furthermore, solid-solution mechanisms should in general lead to higher-rate materials and improved performance.

■ ASSOCIATED CONTENT

📄 Supporting Information

The Supporting Information is available free of charge on the ACS Publications website at DOI: [10.1021/acs.chemmater.6b00319](https://doi.org/10.1021/acs.chemmater.6b00319).

The electrochemistry recorded during the in situ XRD experiments and the points in the electrochemistry at which the diffraction patterns were collected; three individual in situ XRD patterns, Rietveld refinements, and difference plots of LiFePO_4 at different states of charge; XRD patterns of $\text{LiFe}_x\text{Co}_{1-x}\text{PO}_4$ ($0 \leq x \leq 1$); SEM image of a LiFePO_4 composite electrode and particle size analysis and SEM images of as-synthesized LiCoPO_4 ; discharge capacities obtained during the in situ XRD studies; electrochemical data collected during the in situ XRD experiments; ex situ ^{31}P NMR spectra at the end of the first charge for $\text{LiFe}_x\text{Co}_{1-x}\text{PO}_4$ ($0 \leq x \leq 1$); individual XRD patterns at different states of charge for the Fe-rich materials ($x = 1, 0.95, 0.875$); evidence for the formation of the fully delithiated $\text{Fe}_{0.25}\text{Co}_{0.75}\text{PO}_4$ phase at the end of the second charge; concentration profile along the a axis of the 100 nm particle used in the simulation; XRD patterns for the first charge; the a , b , and c unit cell parameters for $\text{LiFe}_x\text{Co}_{1-x}\text{PO}_4$, $\text{Fe}_x\text{Co}_{1-x}\text{PO}_4$, $\text{Li}_{1-x}\text{Fe}_x\text{Co}_{1-x}\text{PO}_4$, and $\text{Li}_{2/3}\text{Fe}_x\text{Co}_{1-x}\text{PO}_4$ ($0 \leq x \leq 1$) as functions of Fe content; percentage change in the lattice parameters compared

with LiFePO_4 for $\text{LiFe}_x\text{Co}_{1-x}\text{PO}_4$, $\text{Fe}_x\text{Co}_{1-x}\text{PO}_4$, $\text{Li}_{1-x}\text{Fe}_x\text{Co}_{1-x}\text{PO}_4$, and $\text{Li}_{2/3}\text{Fe}_x\text{Co}_{1-x}\text{PO}_4$ ($0 \leq x \leq 1$) and the a , b , and c lattice parameter variations, plotted as populations densities, as functions of scan number for all of the reactions discussed in this paper (PDF)

■ AUTHOR INFORMATION

Corresponding Author

*E-mail: cpg27@cam.ac.uk.

Present Addresses

[†]H.L.: X-ray Science Division, Advanced Photon Source, Argonne National Laboratory, Argonne, Illinois 60439, USA.

[‡]M.L.: Weizmann Institute of Science, Rehovot 76100, Israel.

Notes

The authors declare no competing financial interest.

All the raw data for the XRD can be accessed from the University of Cambridge data repository available at the following DOI link: <http://dx.doi.org/10.17863/CAM.21>.

■ ACKNOWLEDGMENTS

We thank the EPSRC for a Doctoral Training Partnership Award and the Department of Energy for support via the NorthEast Center for Chemical Energy Storage, an Energy Frontier Research Center funded by the U.S. Department of Energy, Office of Science, Office of Basic Energy Sciences under Award DE-SC0012583 (support to F.C.S.). We thank the EU for funding from European FP7-265368 via the Euroion Project and the Cambridge Overseas Trust (H.L.) and a Marie Curie

Intra-European Fellowship (M.L.). Work done at Argonne and use of the Advanced Photon Source (APS), an Office of Science User Facility operated for the U.S. Department of Energy Office of Science by Argonne National Laboratory, were supported by the U.S. Department of Energy under Contract DE-AC02-06CH11357. We thank Tao Liu for help with SEM; Dr. Xiao Hua, Ieuan Seymour, Dr. Phoebe Allan, and Dr. Sylvia Britto for their help and discussions; Dr. Matthew Suchomel for instrument support; and Dr. Jan Ilavsky for help with the Irena software.

REFERENCES

- (1) Padhi, A. K.; Nanjundaswamy, K. S.; Goodenough, J. B. Phospho-olivines as Positive-Electrode Materials for Rechargeable Lithium Batteries. *J. Electrochem. Soc.* **1997**, *144*, 1188–1194.
- (2) Yonemura, M.; Yamada, A.; Takei, Y.; Sonoyama, N.; Kanno, R. Comparative Kinetic Study of Olivine LiMPO_4 ($M = \text{Fe, Mn}$). *J. Electrochem. Soc.* **2004**, *151*, A1352–A1356.
- (3) Chen, G.; Song, X.; Richardson, T. J. Electron Microscopy Study of the LiFePO_4 to FePO_4 Phase Transition. *Electrochem. Solid-State Lett.* **2006**, *9*, A295–A298.
- (4) Morgan, D.; Van der Ven, A.; Ceder, G. Li Conductivity in Li_xMPO_4 ($M = \text{Mn, Fe, Co, Ni}$) Olivine Materials. *Electrochem. Solid-State Lett.* **2004**, *7*, A30–A32.
- (5) Malik, R.; Burch, D.; Bazant, M.; Ceder, G. Particle Size Dependence of the Ionic Diffusivity. *Nano Lett.* **2010**, *10*, 4123–4127.
- (6) Delmas, C.; Maccario, M.; Croguennec, L.; Le Cras, F.; Weill, F. Lithium deintercalation in LiFePO_4 nanoparticles via a domino-cascade model. *Nat. Mater.* **2008**, *7*, 665–671.
- (7) Yu, Y.-S.; Kim, C.; Shapiro, D. A.; Farmand, M.; Qian, D.; Tyliczszak, T.; Kilcoyne, A. L. D.; Celestre, R.; Marchesini, S.; Joseph, J.; Denes, P.; Warwick, T.; Strobridge, F. C.; Grey, C. P.; Padmore, H.; Meng, Y. S.; Kostecki, R.; Cabana, J. Dependence on Crystal Size of the Nanoscale Chemical Phase Distribution and Fracture in Li_xFePO_4 . *Nano Lett.* **2015**, *15*, 4282–4288.
- (8) Kang, B.; Ceder, G. Battery materials for ultrafast charging and discharging. *Nature* **2009**, *458*, 190–193.
- (9) Lee, K. T.; Kan, W. H.; Nazar, L. F. Proof of Intercrystallite Ionic Transport in LiMPO_4 Electrodes ($M = \text{Fe, Mn}$). *J. Am. Chem. Soc.* **2009**, *131*, 6044–6045.
- (10) Malik, R.; Zhou, F.; Ceder, G. Kinetics of non-equilibrium lithium incorporation in LiFePO_4 . *Nat. Mater.* **2011**, *10*, 587–590.
- (11) Ferguson, T. R.; Bazant, M. Z. Nonequilibrium Thermodynamics of Porous Electrodes. *J. Electrochem. Soc.* **2012**, *159*, A1967–A1985.
- (12) Liu, H.; Strobridge, F. C.; Borkiewicz, O. J.; Wiaderek, K. M.; Chapman, K. W.; Chupas, P. J.; Grey, C. P. Capturing metastable structures during high-rate cycling of LiFePO_4 nanoparticle electrodes. *Science* **2014**, *344*, 1252817.
- (13) Zhang, X.; van Hulzen, M.; Singh, D. P.; Brownrigg, A.; Wright, J. P.; van Dijk, N. H.; Wagemaker, M. Rate-Induced Solubility and Suppression of the First-Order Phase Transition in Olivine LiFePO_4 . *Nano Lett.* **2014**, *14*, 2279–2285.
- (14) Ravnsbæk, D. B.; Xiang, K.; Xing, W.; Borkiewicz, O. J.; Wiaderek, K. M.; Gionet, P.; Chapman, K. W.; Chupas, P. J.; Chiang, Y.-M. Extended Solid Solutions and Coherent Transformations in Nanoscale Olivine Cathodes. *Nano Lett.* **2014**, *14*, 1484–1491.
- (15) Zhang, X.; van Hulzen, M.; Singh, D. P.; Brownrigg, A.; Wright, J. P.; van Dijk, N. H.; Wagemaker, M. Direct view on the phase evolution in individual LiFePO_4 nanoparticles during Li-ion battery cycling. *Nat. Commun.* **2015**, *6*, 8333.
- (16) Shin, H. C.; Park, S. B.; Jang, H.; Chung, K. Y.; Cho, W. I.; Kim, C. S.; Cho, B. W. Rate performance and structural change of Cr-doped LiFePO_4/C during cycling. *Electrochim. Acta* **2008**, *53*, 7946–7951.
- (17) Bramnik, N. N.; Trots, D. M.; Hofmann, H. J.; Ehrenberg, H. Mixed $\text{LiCo}_{0.6}\text{M}_{0.4}\text{PO}_4$ ($M = \text{Mn, Fe, Ni}$) phosphates: cycling mechanism and thermal stability. *Phys. Chem. Chem. Phys.* **2009**, *11*, 3271–3277.
- (18) Omenya, F.; Chernova, N. A.; Zhang, R.; Fang, J.; Huang, Y.; Cohen, F.; Dobrzynski, N.; Senanayake, S.; Xu, W.; Whittingham, M. S. Why Substitution Enhances the Reactivity of LiFePO_4 . *Chem. Mater.* **2013**, *25*, 85–89.
- (19) Park, K. Y.; Hong, J.; Kim, J.; Park, Y. U.; Kim, H.; Seo, D. H.; Kim, S. W.; Choi, J. W.; Kang, K. Factors that Affect the Phase Behavior of Multi-Component Olivine ($\text{LiFe}_x\text{Mn}_y\text{Co}_{1-x-y}\text{PO}_4$; $0 < x, y < 1$) in Lithium Rechargeable Batteries: One-Phase Reaction vs. Two-Phase Reaction. *J. Electrochem. Soc.* **2013**, *160*, A444–A448.
- (20) Hong, J.; Wang, C. S.; Chen, X.; Upreti, S.; Whittingham, M. S. Vanadium Modified LiFePO_4 Cathode for Li-Ion Batteries. *Electrochem. Solid-State Lett.* **2009**, *12*, A33–A38.
- (21) Bramnik, N. N.; Nikolowski, K.; Baetz, C.; Bramnik, K. G.; Ehrenberg, H. Phase Transitions Occurring upon Lithium Insertion–Extraction of LiCoPO_4 . *Chem. Mater.* **2007**, *19*, 908–915.
- (22) Ehrenberg, H.; Bramnik, N. N.; Senyshyn, A.; Fuess, H. Crystal and magnetic structures of electrochemically delithiated $\text{Li}_{1-x}\text{CoPO}_4$ phases. *Solid State Sci.* **2009**, *11*, 18–23.
- (23) Bramnik, N. N.; Bramnik, K. G.; Baetz, C.; Ehrenberg, H. Study of the effect of different synthesis routes on Li extraction–insertion from LiCoPO_4 . *J. Power Sources* **2005**, *145*, 74–81.
- (24) Strobridge, F. C.; Clément, R. J.; Leskes, M.; Middlemiss, D. S.; Borkiewicz, O. J.; Wiaderek, K. M.; Chapman, K. W.; Chupas, P. J.; Grey, C. P. Identifying the Structure of the Intermediate, $\text{Li}_{2/3}\text{CoPO}_4$ Formed during Electrochemical Cycling of LiCoPO_4 . *Chem. Mater.* **2014**, *26*, 6193–6205.
- (25) Kobayashi, G.; Nishimura, S.-I.; Park, M.-S.; Kanno, R.; Yashima, M.; Ida, T.; Yamada, A. Isolation of Solid Solution Phases in Size-Controlled Li_xFePO_4 at Room Temperature. *Adv. Funct. Mater.* **2009**, *19*, 395–403.
- (26) Borkiewicz, O. J.; Shyam, B.; Wiaderek, K. M.; Kurtz, C.; Chupas, P. J.; Chapman, K. W. The AMPIX electrochemical cell: a versatile apparatus for in situ X-ray scattering and spectroscopic measurements. *J. Appl. Crystallogr.* **2012**, *45*, 1261–1269.
- (27) Lee, P. L.; Shu, D.; Ramanathan, M.; Preissner, C.; Wang, J.; Beno, M. A.; Von Dreere, R. B.; Ribaud, L.; Kurtz, C.; Antao, S. M.; Jiao, X.; Toby, B. H. A twelve-analyzer detector system for high-resolution powder diffraction. *J. Synchrotron Radiat.* **2008**, *15*, 427–432.
- (28) Stinton, G. W.; Evans, J. S. O. Parametric Rietveld refinement. *J. Appl. Crystallogr.* **2007**, *40*, 87–95.
- (29) Jarvinen, M. Application of Symmetrized Harmonics Expansion to Correction of the Preferred Orientation Effect. *J. Appl. Crystallogr.* **1993**, *26*, 525–531.
- (30) Popa, N. C. Texture in Rietveld Refinement. *J. Appl. Crystallogr.* **1992**, *25*, 611–616.
- (31) Coelho, A. A. A charge-flipping algorithm incorporating the tangent formula for solving difficult structures. *Acta Crystallogr., Sect. A: Found. Crystallogr.* **2007**, *63*, 400–406.
- (32) Warren, B. E. *X-ray Diffraction*; Addison-Wesley: Reading, MA, 1969.
- (33) Rudman, P. S. An X-ray Diffraction Method for the Determination of Composition Distribution in Inhomogeneous Binary Solid Solution. *Acta Crystallogr.* **1960**, *13*, 905–909.
- (34) Kang, H.-C.; Jun, D.-K.; Jin, B.; Jin, E. M.; Park, K.-H.; Gu, H.-B.; Kim, K.-W. Optimized solid-state synthesis of LiFePO_4 cathode materials using ball-milling. *J. Power Sources* **2008**, *179*, 340–346.
- (35) Yang, X.; Liu, D.; Xu, X.; He, X.; Xie, J. Mechanism and kinetic studies on the synthesis of LiFePO_4 via solid-state reactions. *CrystEngComm* **2013**, *15*, 10648–10656.
- (36) Tarascon, J. M.; Guyomard, D. New electrolyte compositions stable over the 0 to 5 V voltage range and compatible with the $\text{Li}_{1+x}\text{Mn}_2\text{O}_4/\text{carbon}$ Li-ion cells. *Solid State Ionics* **1994**, *69*, 293–305.
- (37) Guyomard, D.; Tarascon, J. M. High voltage stable liquid electrolytes for $\text{Li}_{1+x}\text{Mn}_2\text{O}_4/\text{carbon}$ rocking-chair lithium batteries. *J. Power Sources* **1995**, *54*, 92–98.
- (38) Snook, G. A.; Huynh, T. D.; Hollenkamp, A. F.; Best, A. S. Rapid SECM probing of dissolution of LiCoO_2 battery materials in an ionic liquid. *J. Electroanal. Chem.* **2012**, *687*, 30–34.

(39) Bai, P.; Cogswell, D. A.; Bazant, M. Z. Suppression of Phase Separation in LiFePO_4 Nanoparticles During Battery Discharge/. *Nano Lett.* **2011**, *11*, 4890–4896.

(40) Meethong, N.; Huang, H.-Y. S.; Carter, W. C.; Chiang, Y.-M. Size-Dependent Lithium Miscibility Gap in Nanoscale $\text{Li}_{1-x}\text{FePO}_4$. *Electrochem. Solid-State Lett.* **2007**, *10*, A134–A138.

(41) Molenda, J.; Kulka, A.; Milewska, A.; Zając, W.; Świerczek, K. Structural, Transport and Electrochemical Properties of LiFePO_4 Substituted in Lithium and Iron Sublattices (Al, Zr, W, Mn, Co and Ni). *Materials* **2013**, *6*, 1656–1687.

(42) Nytén, A.; Thomas, J. O. A neutron powder diffraction study of $\text{LiCo}_x\text{Fe}_{1-x}\text{PO}_4$ for $x = 0, 0.25, 0.40, 0.60$ and 0.75 . *Solid State Ionics* **2006**, *177*, 1327–1330.

(43) Shannon, R. D. Revised Effective Ionic Radii and Systematic Studies of Interatomic Distances in Halides and Chalcogenides. *Acta Crystallogr., Sect. A: Cryst. Phys., Diffr., Theor. Gen. Crystallogr.* **1976**, *32*, 751–767.